Observations of Internal Tides on the Oregon Continental Slope

KIM I. MARTINI, MATTHEW H. ALFORD, AND ERIC KUNZE

Applied Physics Laboratory and School of Oceanography, University of Washington, Seattle, Washington

SAMUEL M. KELLY AND JONATHAN D. NASH

College of Oceanic and Atmospheric Sciences, Oregon State University, Corvallis, Oregon

(Manuscript received 16 September 2010, in final form 19 April 2011)

ABSTRACT

A complex superposition of locally forced and shoaling remotely generated semidiurnal internal tides occurs on the Oregon continental slope. Presented here are observations from a zonal line of five profiling moorings deployed across the continental slope from 500 to 3000 m, a 24-h expendable current profiler (XCP) survey, and five 15–48-h lowered ADCP (LADCP)/CTD stations. The 40-day moored deployment spans three spring and two neap tides, during which the proportions of the locally and remotely forced internal tides vary. Baroclinic signals are strong throughout spring and neap tides, with 4–5-day-long bursts of strong cross-slope baroclinic semidiurnal velocity ($u_{M_2} > 0.05$ m s^{-1}) and vertical displacement ($\zeta_{M_2} > 100$ m). Energy fluxes exhibit complex spatial and temporal patterns throughout both tidal periods. During spring tides, local barotropic forcing is strongest and energy flux over the slope is predominantly offshore (westward). During neap tides, shoaling remotely generated internal tides dominate and energy flux is predominantly onshore (eastward). Shoaling internal tides do not exhibit a strong spring–neap cycle and are also observed during the first spring tide, indicating that they originate from multiple sources. The bulk of the remotely generated internal tide is hypothesized to be generated from south of the array (e.g., Mendocino Escarpment), because energy fluxes at the deep mooring 100 km offshore are always directed northward. However, fluxes on the slope suggest that the northbound internal tide is turned onshore, most likely by reflection from large-scale bathymetry. This is verified with a simple three-dimensional model of mode-1 internal tides propagating obliquely onto a near-critical slope, whose output conforms fairly well to observations, in spite of its simplicity.

1. Introduction

When astronomically forced barotropic tides flow over bathymetric features, they generate baroclinic internal tides. The conversion is particularly efficient when barotropic flow is directed across large bathymetric obstacles (St. Laurent et al. 2003; Garrett and Kunze 2007), such as the Hawaiian Ridge (Ray and Cartwright 2001; Merrifield et al. 2001; Rudnick et al. 2003), the Aleutian Ridge (Cummins et al. 2001), and Mendocino Escarpment (Althaus et al. 2003), but also occurs over small-scale bathymetric roughness (Bell 1975; St. Laurent and Garrett 2002; Legg 2004; Nash et al. 2007). For large obstacles, a small fraction of the barotropic tide is converted to high modes, whereas the bulk is converted into low modes (Nash et al. 2006). Because of their low shear and large group speeds, low-mode internal tides radiate far from generation sites (>1000 km) (Ray and Mitchum 1997; Cummins et al. 2001; Ray and Cartwright 2001; Alford 2003; Simmons et al. 2004; Zhao and Alford 2009) and have been observed impinging on continental slopes (Nash et al. 2004). Eventually, internal tides may dissipate either through interactions with rough and abrupt topography (Moum et al. 2002) or parametric subharmonic instability (MacKinnon and Winters 2005), but it has not yet been established which process is most important. In a global assessment using Gregg–Henyey scaling, Kunze et al. (2006) could not account for the deep-ocean tidal dissipation predicted by Egbert and Ray (2003), but sampling was sparse and particularly lacked data on continental slopes. Understanding the geography and relative importance of these processes is a central task to finding

Corresponding author address: Kim Martini, Ocean Physics Department, Applied Physics Laboratory, 1013 NE 40th Street, Seattle, WA 98105.
E-mail: martini@apl.washington.edu

DOI: 10.1175/2011JPO4581.1

the eventual fate of the global semidiurnal internal tide.

The rough and near-critical Oregon continental slope may be a potential sink for low-mode internal tides. Moum et al. (2002) reported elevated dissipation rates ϵ exceeding 10^{-8} W kg^{-1}, whereas Nash et al. (2007) observed turbulent semidiurnal "hotspots" with $\epsilon > 10^{-7}$ W kg^{-1}. These dissipation rates are of similar magnitude to other locations with rough bathymetry such as the Mid-Atlantic Ridge (Ledwell et al. 2000; St. Laurent and Garrett 2002; Thurnherr et al. 2005). On the Virginia continental slope, shoaling low-mode tides were observed, but dissipation was weaker, $\epsilon < 10^{-8}$ W kg^{-1} (Nash et al. 2004). Bathymetry on the Oregon slope is substantially rougher and also closer to critical than the Virginia slope, possibly contributing to its elevated dissipation. On the Oregon slope, enhanced turbulence is hypothesized to be forced by either the dissipation of (i) low-mode internal tides that shoal onto the slope from a remote source, (ii) internal tides generated locally over small-scale bathymetric roughness on the slope, or (iii) a combination of the two.

In this paper, we describe the semidiurnal internal tide on the Oregon continental slope using data from a densely instrumented array designed to capture shoaling low-mode internal tides. Although barotropic velocities are primarily along-isobath on the slope, observations and numerical simulations suggest internal tides are also generated locally. When superposed, internal tides from local and remote sources cannot be easily distinguished. If standing or partly standing internal tides form between locally generated and shoaling internal tides, energy flux may be perpendicular to the direction of wave propagation (Nash et al. 2004; Martini et al. 2007). Thus, interpretation of a multidirectional wave field can be challenging.

To aid in interpretation of the multidirectional internal tide, we partition the observations into semidiurnal spring and neap tides, when local barotropic forcing is strong and weak, respectively. During spring tides, energy flux is usually offshore, suggesting the observed wave field is dominated by local barotropic forcing at either small-scale bathymetric features or the shelf break. During neaps, energy flux is predominantly onshore, suggesting remote sources. Therefore the Oregon continental slope is both a source and sink of semidiurnal internal tides.

Internal tides observed during local spring and neap tides are dominated by local barotropic forcing and propagation from remote sources, respectively. However, because shoaling internal tides have no particular spring–neap cycle, remotely and locally generated internal tides often superpose (i.e., during the first spring tide), creating a complex, multidirectional wave field. In addition, remotely generated internal tides are obliquely incident on the slope, turning onshore after reflection. In the following, remotely generated internal tides are disentangled from locally generated internal tides using a new technique described in section 5b and by comparing our observations to a simple model of obliquely incident internal tides reflecting from a slope (section 5d).

This paper is organized as follows: The instrument array and techniques used to extract the semidiurnal internal tides from observations are discussed in sections 2 and 3, respectively. Observations are presented in section 4. The local and remote wave field, sources of the remote wave field, and a simple theoretical model of internal tides shoaling onto a supercritical slope are discussed in section 5. Conclusions are presented in section 6.

2. Instrumentation

a. Moored array

A zonal line of five moorings was deployed at 43°12′N for 40 days during September–October 2005 (Fig. 1). The array spanned the Oregon continental slope from 500 to 3000 m water depth at 8.5-km intervals plus a deep-ocean mooring 100 km offshore. Each mooring was instrumented with a McLane moored profiler (MMP) to acquire nearly full-depth profiles of horizontal velocity, temperature, and conductivity. Traveling at a mean speed of 25 cm s^{-1} (900 m h^{-1}), the profilers completed a single up or down profile in 0.5–2.2 h. Pre- and post-deployment calibrations were performed on all MMP conductivity–temperature–depth (CTD) sensors and compasses. Corrections were made for clock drift (<2 min in all cases).

To measure velocity in the upper 50 m, above the profiling range of the MMP, upward-looking RDI ADCPs were placed at the tops of moorings MP3 and MP5. The ADCPs sampled every 30 min in 2-m vertical bins. The offshore moored profiler (MP1) only profiled the upper 2000 m, but an Aanderaa RCM8 current meter and a Seabird SBE 37-SM Microcat conductivity, temperature, and pressure recorder placed 39 m above the bottom allow the resolution of modes 1 and 2. To resolve higher-frequency variations, Microcat and Microcat/Seabird SBE 39 temperature recorder pairs were placed at the top (~50 m below the surface) and bottom (~20 m above the seafloor) of each mooring, respectively.

A summary of raw velocity data from all five moorings is presented in Fig. 2. At mooring MP3, because of heavy ballasting, the MMP stopped profiling the upper water column after yearday 265 (Fig. 2c) and then stopped altogether after 30 days. Data from MP6 are not used here, because the MMP stopped sampling the upper water column after 12 days and was accidentally caught by a fishing vessel 10 days later.

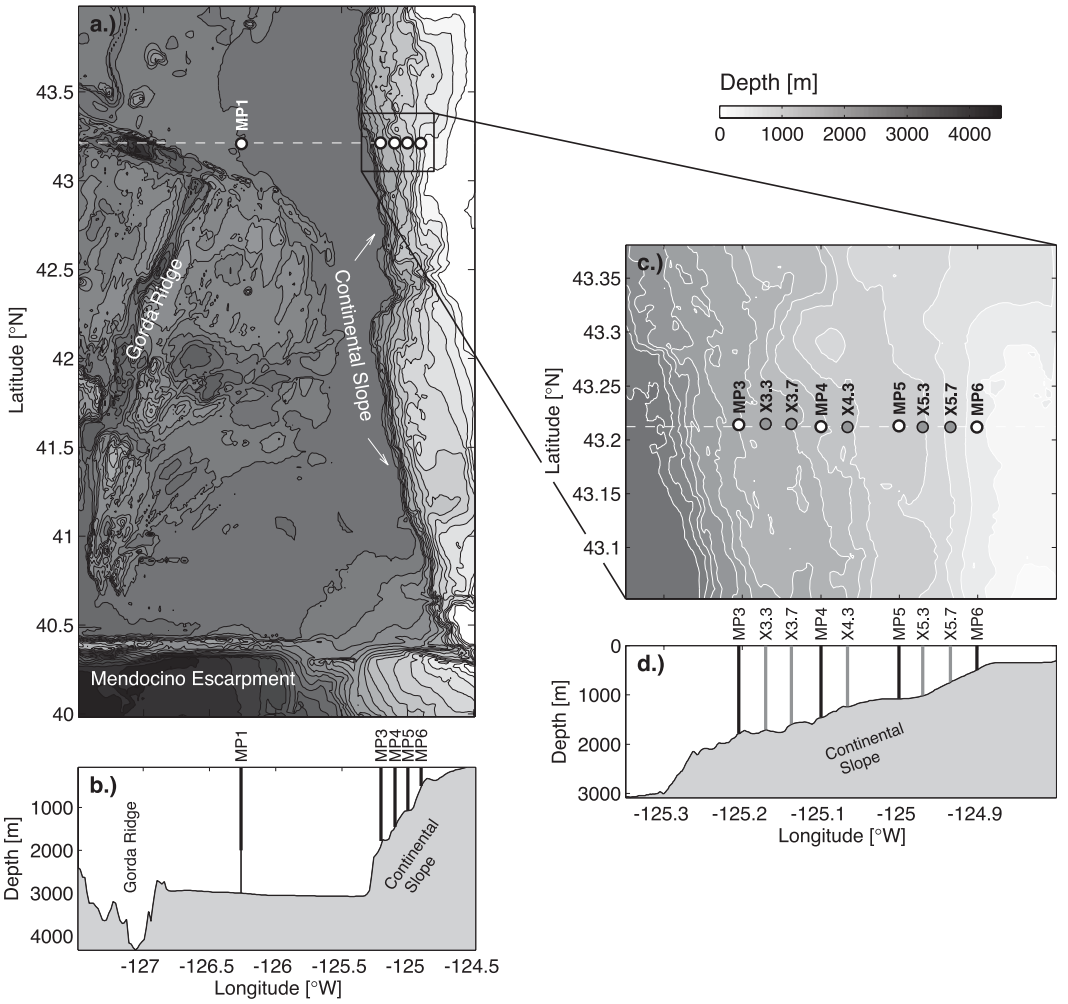

FIG. 1. (a) Plan-view map of Oregon continental slope bathymetry with major topographic features. The moorings (white circles) lie along 43.2°N, which is marked by a white dashed line. The offshore mooring, MP1, is labeled in white. (b) Bathymetric cross section taken along 43.2°N. MP1 only profiles the upper 2000 m, as denoted by the thick black line. (c) Zoomed slope bathymetry with moorings (white circles) and XCP stations (gray circles) labeled. (d) Zoomed cross section of slope with moorings (black lines) and XCP profiles (gray lines).

b. XCP survey

To better resolve the spatial structure of the internal wave field on the slope, expendable current profilers (XCPs) were dropped every 3 h over one 24-h time period along the mooring line at six stations (Figs. 1a,d). Each XCP obtains temperature and absolute velocity to depths of 2000 m when referenced to the shipboard ADCP.

c. LADCP/CTD time series

By cycling the shipboard CTD from the surface to the bottom every 3 h, 15–48-h time series of salinity, temperature, and pressure profiles were obtained at eight stations. A pair of upward-/downward-looking 300-kHz RDI lowered ADCPs (LADCPs) attached to the CTD cage measured full-depth velocity profiles, operating below 2000 m, beyond the XCP's reach.

3. Methods

a. Extraction of the semidiurnal wave field

Spectral analysis of velocity, temperature, and salinity data from the ADCP, Aanderaa, and Microcats indicate there are three dominant periodic signals on the Oregon slope: M_2 (12.42 h), K_1 (23.94 h), and inertial (17.48 h). To ensure that the MMP's uneven temporal sampling (~3 h at the top and bottom and ~1.5 at middepth) does not alias the semidiurnal signals, harmonic fits are employed (appendix A). To distinguish the three frequencies, 3.5-day sliding windowed fits are computed at 2-h

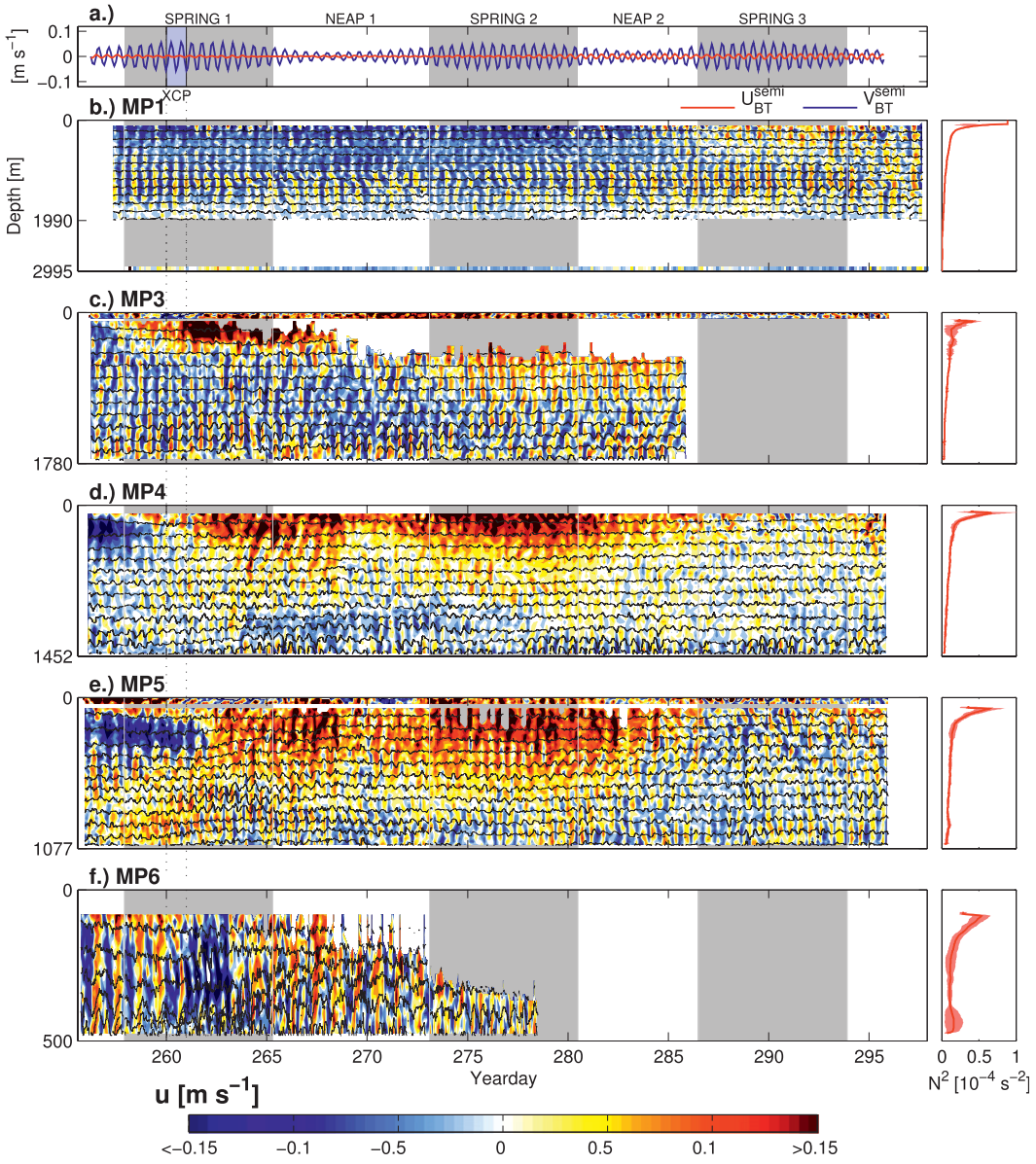

FIG. 2. (a) Semidiurnal barotropic zonal (red) and meridional (blue) velocities at midslope (MP4). (b)–(f) Depth–time series of zonal (across shore) velocity (shading) and isopycnal depths (black lines) at moorings MP1–MP5 from the surface ($z = 0$) to the local water depth ($z = -H$). Onshore velocities (positive) are red, whereas offshore velocities (negative) are blue. The 18-h XCP survey at yearday 260 is demarked by the vertical black dotted lines. MP1 is the offshore mooring, and MP3–MP5 are located on the continental slope. Mean stratifications from the MMPs over the entire deployment (red line) and their two standard deviation spreads (red shading) is to the right. At MP1, stratification below the range of the MMP is filled in using shipboard CTD data. Throughout the figures, gray intervals denote local spring tides and white intervals denote local neaps.

intervals (each window incorporating a new profile) at each depth for both horizontal velocity and vertical displacement to resolve slowly varying phase shifts throughout the deployment. This technique does not separate the M_2 and S_2 tides but does capture their 14-day spring–neap cycle.

Figure 3 demonstrates the separation into each band at MP4. Because the moorings are above the turning latitude for diurnal internal tides, the K_1 signal is primarily barotropic (Fig. 3e). Upward phase propagation near yearday 264 at near-inertial frequencies (Fig. 3f) is associated with a downward-propagating wave packet.

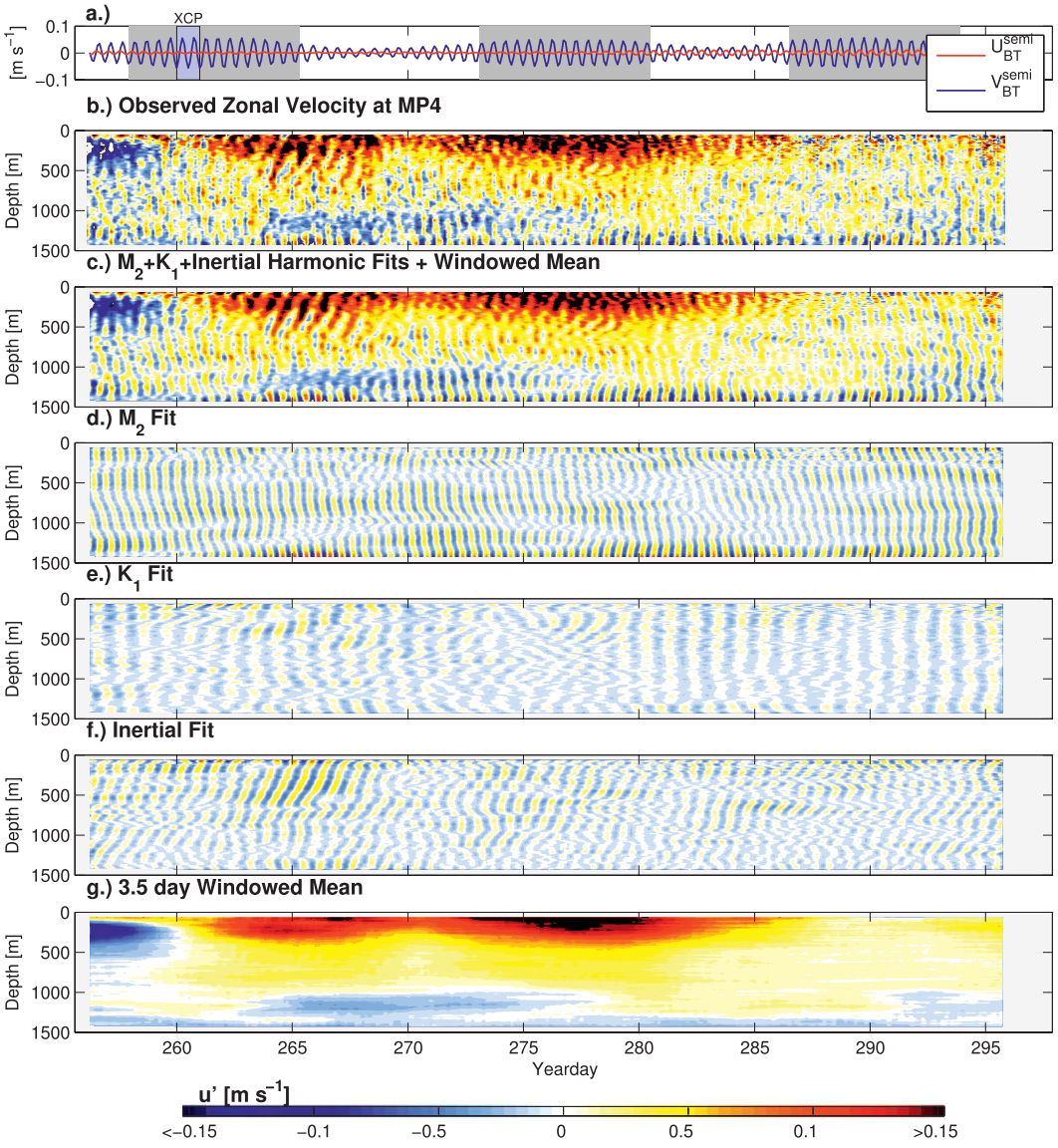

FIG. 3. Decomposition of zonal velocity into the three dominant bands: (a) semidiurnal barotropic zonal (red) and meridional (blue) velocities at the midslope mooring MP4; (b) observed zonal velocity at MP4; and (c) sum of the 3.5-day windowed fits to the M_2, K_1, and inertial harmonics plus the mean velocity over each 3.5-day window (windowed mean). Also shown are the separated zonal (d) semidiurnal, (e) diurnal, (f) inertial, and (g) windowed-mean (which includes low-frequency variability) velocity fields.

Because winds prior to this period were weak (not shown), it is possible that the packet was generated by geostrophic adjustment of an energetic northward-flowing filament. Alternatively, it is possible the packet is trapped inside an eddy (Fig. 3g) (Kunze 1985). This paper will focus only on the semidiurnal signal hereafter.

b. Isopycnal displacements and vertical velocity

To calculate baroclinic pressure perturbations, energy fluxes, and potential energy densities, vertical isopycnal displacements must first be determined. Isopycnal displacements $\zeta(z, t)$ are defined from the MMP potential density data as the vertical distance an isopycnal is displaced from its mean depth following Desaubies and Gregg (1981); for the XCP data, the vertical displacements are relative to the mean temperature profile. A time-mean isopycnal depth profile $\overline{z(\sigma_\theta)}$ for the entire deployment is computed at each mooring to account for horizontal variations in the density profiles. Isopycnal slopes decrease moving onshore and are largest at the surface. Linear interpolation is used to find isopycnal depths $z(\sigma_\theta, t)$ from which vertical displacements are

calculated, $\zeta(z,t) = z(\sigma_\theta, t) - \overline{z(\sigma_\theta)}$. Mean potential density profiles $\overline{\sigma_\theta}$ slowly change over the course of the deployment, causing vertical displacement biases <30 m, reducing to <5 m for the semidiurnal signal.

Semidiurnal vertical velocities are found from vertical displacement harmonic fits,

$$w' = \partial\zeta(z,t)/\partial t = \zeta_0 \omega_{M_2} \sin(\omega_{M_2} t - \phi_\zeta), \quad (1)$$

where ζ_0 is vertical displacement amplitude, ω_{M_2} is the semidiurnal frequency, and ϕ_ζ is the vertical displacement phase.

c. Energy density and flux

The energy density is the sum of horizontal kinetic energy,

$$\mathrm{HKE}(z) = \frac{\rho_0}{2}\langle u'^2 + v'^2\rangle_t, \quad (2)$$

and available potential energy,

$$\mathrm{APE}(z) = \frac{\rho_0}{2}\overline{N}^2(z)\langle \zeta^2\rangle_t, \quad (3)$$

where ρ_0 is the depth-averaged density, u' is the zonal baroclinic velocity, v' is the meridional baroclinic velocity, and $\overline{N}^2(z)$ is the time-mean stratification profile. Here, $\langle\ \rangle_t$ denotes averaging over one wave period. For a single, freely propagating internal wave, horizontal kinetic energy is always larger than available potential energy (Fofonoff 1969).

Horizontal energy flux is the product of the horizontal baroclinic velocity and the pressure perturbation averaged over a wave period,

$$\mathbf{F} = \langle \mathbf{u}' p' \rangle_t, \quad (4)$$

where p' is the pressure perturbation. Similarly, vertical energy flux is

$$F_z = \langle w' p' \rangle_t. \quad (5)$$

Following Althaus et al. (2003), the pressure perturbation is calculated from vertical displacements such that

$$p' = -\rho_0 \int_z^0 \overline{N}^2(z)\zeta(z)\, dz - \overline{p'}. \quad (6)$$

To satisfy the baroclinicity condition (the depth mean of the baroclinic pressure perturbation is zero), the depth mean of the pressure perturbation, $\overline{p'} = \rho_0 \int_{-H}^0 \int_z^0 N^2 \zeta(z)\, dz^*\, dz$, must be removed (Kunze et al. 2002). Gerkema and van Haren (2007) invalidated this condition over a sloping bottom but neglected horizontal-momentum loss to the generation of internal waves (i.e., wave drag). Recently, Kelly et al. (2010) revalidated the baroclinicity condition by including wave drag. Surface gaps and baroclinic aliasing do not greatly affect the determination of energy flux (appendix A).

At the offshore mooring, MP1, mode-1 and mode-2 velocities, vertical displacements, and pressure are found by linear regression using theoretical flat-bottomed modes. To obtain higher modes, low modes are subtracted from the total semidiurnal values. Energy density, horizontal energy flux, and vertical energy flux for both low and high modes are then calculated. Low-mode depth-integrated energy densities and fluxes presented for MP1 are full depth (0–2995 m), whereas the high-mode values can only be computed over the profiling range (50–2000 m).

4. Observations

a. Moored profiler time series

1) Semidiurnal barotropic tide

Observed semidiurnal zonal velocities $u^{\mathrm{semi}}(z, t)$ are the sum of barotropic $U_{\mathrm{BT}}^{\mathrm{semi}}(t)$ and baroclinic $u'^{\mathrm{semi}}(z, t)$ velocities,

$$u^{\mathrm{semi}}(z,\ t) = U_{\mathrm{BT}}^{\mathrm{semi}}(t) + u'^{\mathrm{semi}}(z,t), \quad (7)$$

where barotropic velocities are defined as the depth mean of the observed velocity at time t,

$$U_{\mathrm{BT}}^{\mathrm{semi}}(t) = \frac{1}{H}\int_{-H}^0 u^{\mathrm{semi}}(z,t)\, dz, \quad (8)$$

and H is the water depth. Sampling rates of MMPs are sufficient to accurately determine the semidiurnal barotropic velocity (appendix A) as verified against LADCP data.

Smoothed isobaths on the Oregon continental slope run nearly north–south such that positive zonal velocities $u(z, t)$ are eastward and upslope, while positive meridional velocities $v(z, t)$ are northward and along isobath. At all moorings (shown here only at MP4 in Fig. 4), barotropic semidiurnal velocities are strongest in the meridional direction (Fig. 4b), whereas baroclinic semidiurnal velocities are strongest in the zonal direction (Fig. 4a). Meridional barotropic velocities have a strong spring–neap cycle, whereas barotropic zonal velocities do not. Baroclinic velocities generally lack a spring–neap cycle and are not phase locked to barotropic velocities. These properties are associated with a remotely generated internal tide from either distant or multiple sources.

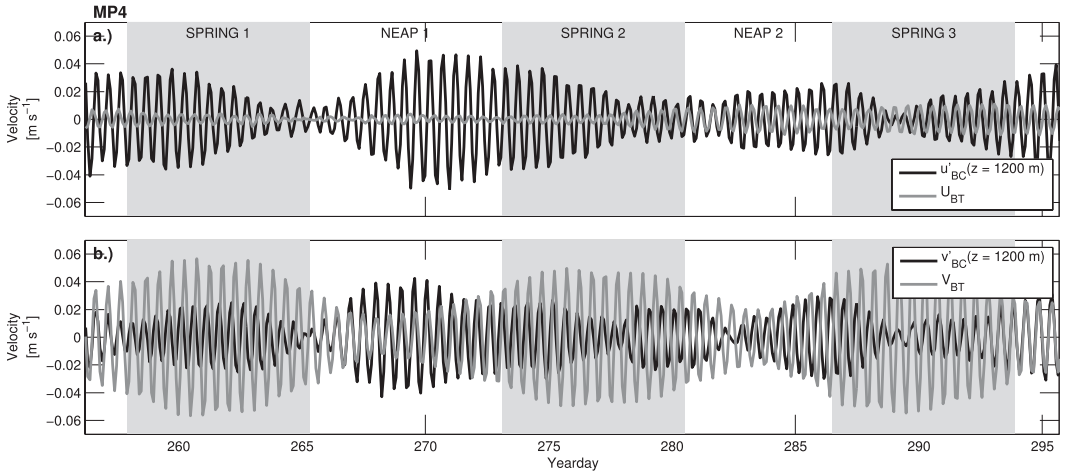

FIG. 4. Semidiurnal barotropic (gray lines) and baroclinic velocities at 1200 m (black line) in the (a) zonal and (b) meridional directions at the midslope mooring MP4. Barotropic velocities dominate in the meridional direction (gray), whereas baroclinic velocities dominate in the zonal direction (black).

2) BAROCLINIC VELOCITY AND VERTICAL DISPLACEMENT

The semidiurnal internal tide on the Oregon continental slope varies significantly over the 40-day mooring deployment (Figs. 5c–e). All moorings show 4–5-day bursts of enhanced baroclinic velocity ($u'_{M_2} > 0.05$ m s^{-1}) and vertical displacements ($\zeta'_{M_2} > 100$ m), predominantly within 500 meters above bottom (mab), but they evolve differently at each mooring. At MP3, these bursts develop near the seafloor and spread upward over the course of the burst. At MP4, the bursts remain near the bottom. Enhanced velocities and vertical displacements do not occur simultaneously at all moorings on the slope, indicating the internal tide is spatially and temporally heterogeneous.

3) ENERGY FLUX

Semidiurnal zonal (left column) and meridional fluxes (right column) at moorings MP1–MP5 are presented in Fig. 6. Throughout the deployment, the magnitude and direction of semidiurnal energy flux vary both temporally and spatially across the array but have several defining characteristics.

On the slope, fluxes are strongest near the bottom (Figs. 6b–e,g–j). Bottom-intensified flux is consistent with a shoaling internal tide (Wunsch 1968, 1969) or local generation. The direction of bottom-intensified zonal fluxes (<300 mab) at MP3–MP5 show a pronounced spring–neap cycle. During local neaps, zonal flux is predominantly onshore. During local spring tides, flux is predominantly offshore. The exception is the first local spring tide. After the peak of the first spring tide (yearday 261), near-bottom flux changes direction and suggests a significant change in the composition of the internal tide.

Above the bottom-intensified layer, there are no strong temporal flux patterns. Weaker patterns exist (e.g., onshore flux at 500-m depth during local spring tides at MP3) but do not match the near-bottom flux patterns.

Similar to near-bottom fluxes, fluxes integrated over the entire water column at MP4 and MP5 are predominantly onshore during neaps and either offshore or weakly onshore during spring tides (Fig. 7). Depth-integrated fluxes at MP3 during neaps and springs 2 and 3 are not full depth because the MMP was unable to travel above 500-m depth after yearday 270 but still follow the same directional pattern. When the local barotropic forcing is large during the first spring tide, full-depth-integrated fluxes are strongly onshore, suggesting it is different from the second and third spring tides. Differences between spring tides may be attributed to remotely generated internal tides and their modulation of local internal tide generation (Kelly and Nash 2010).

At the offshore mooring, MP1, flux is predominantly meridional, lacks a spring–neap cycle, and does not correlate well with fluxes on the slope (Figs. 6a,g). Flux is intensified and generally northward in the upper 1000 m above the mode-1 zero crossing (at approximately 1200 m). Starting at yearday 265, there is a persistent, relatively stronger narrow band of southwestward energy flux at 1000 m that may originate from the slope.

b. Spring and neap tides

The alternation between offshore flux during spring tide and onshore flux during neap suggests that the observed internal tide originates at more than one source. Based upon these observations, we divide the time series into three spring and two neap tide intervals (shown in

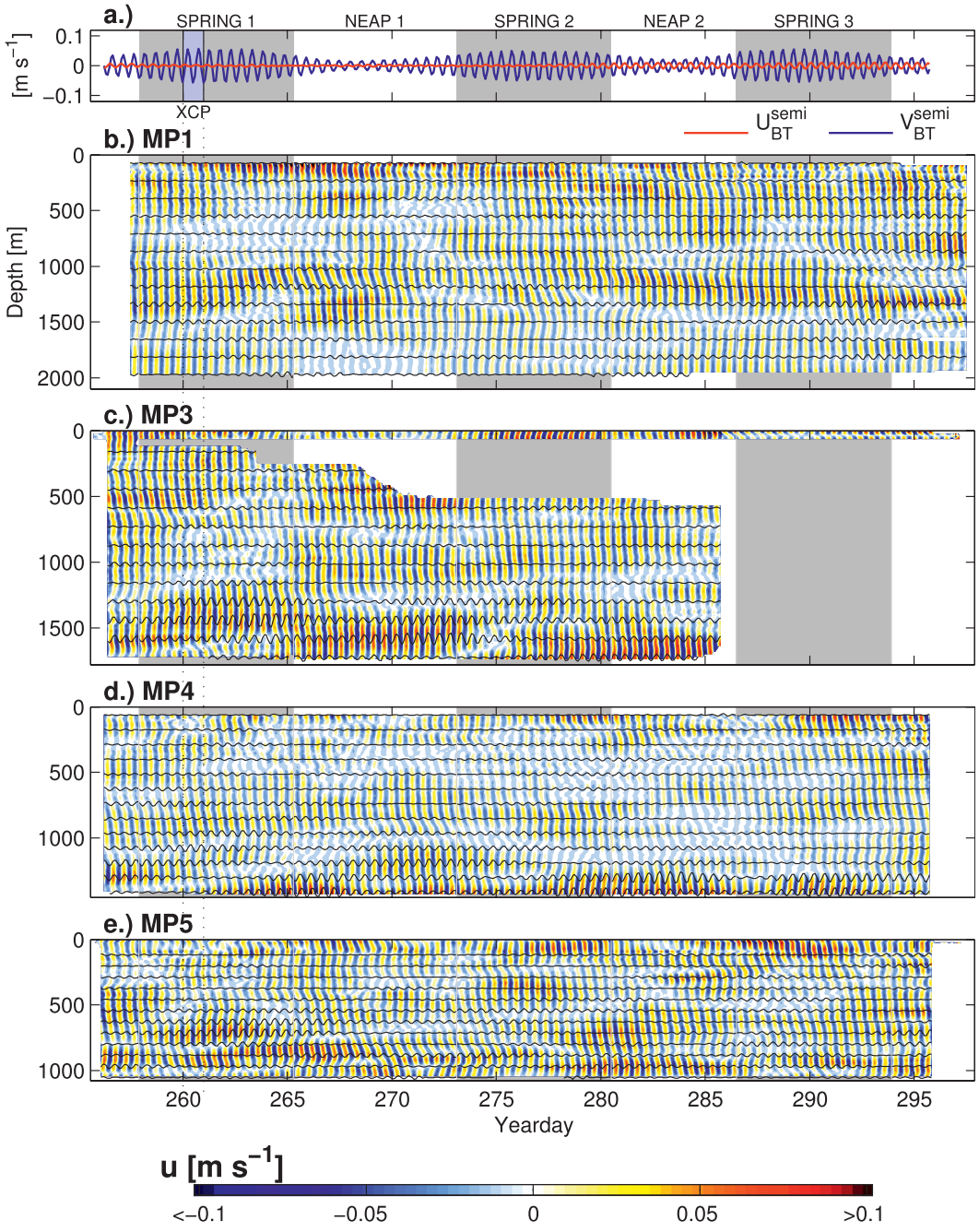

FIG. 5. Semidiurnal wave field at all moorings: (a) semidiurnal barotropic zonal (red) and meridional (blue) velocities at midslope (MP4) and (b)–(f) semidiurnal zonal velocity (shading) and isopycnal displacements (black lines) at moorings MP1–MP5.

all figures as gray and white regions, respectively), which are referred to here as springs 1, 2, and 3 and neaps 1 and 2 (Fig. 2a). The first spring tide is further subdivided into spring 1a and 1b, because intervals of both onshore and offshore fluxes are observed during the period.

Differences between spring and neap tides are more clearly seen when divided into maps of 300-mab depth-integrated energy flux (Fig. 8) and across-slope vertical energy flux (Fig. 9), averaged over each spring or neap tide interval. During neaps, bottom-intensified onshore fluxes are upward at MP3 and MP4 (Figs. 9b,f). During spring tides, offshore fluxes are upward, except at MP4, where they are offshore and downward (Figs. 9a,d).

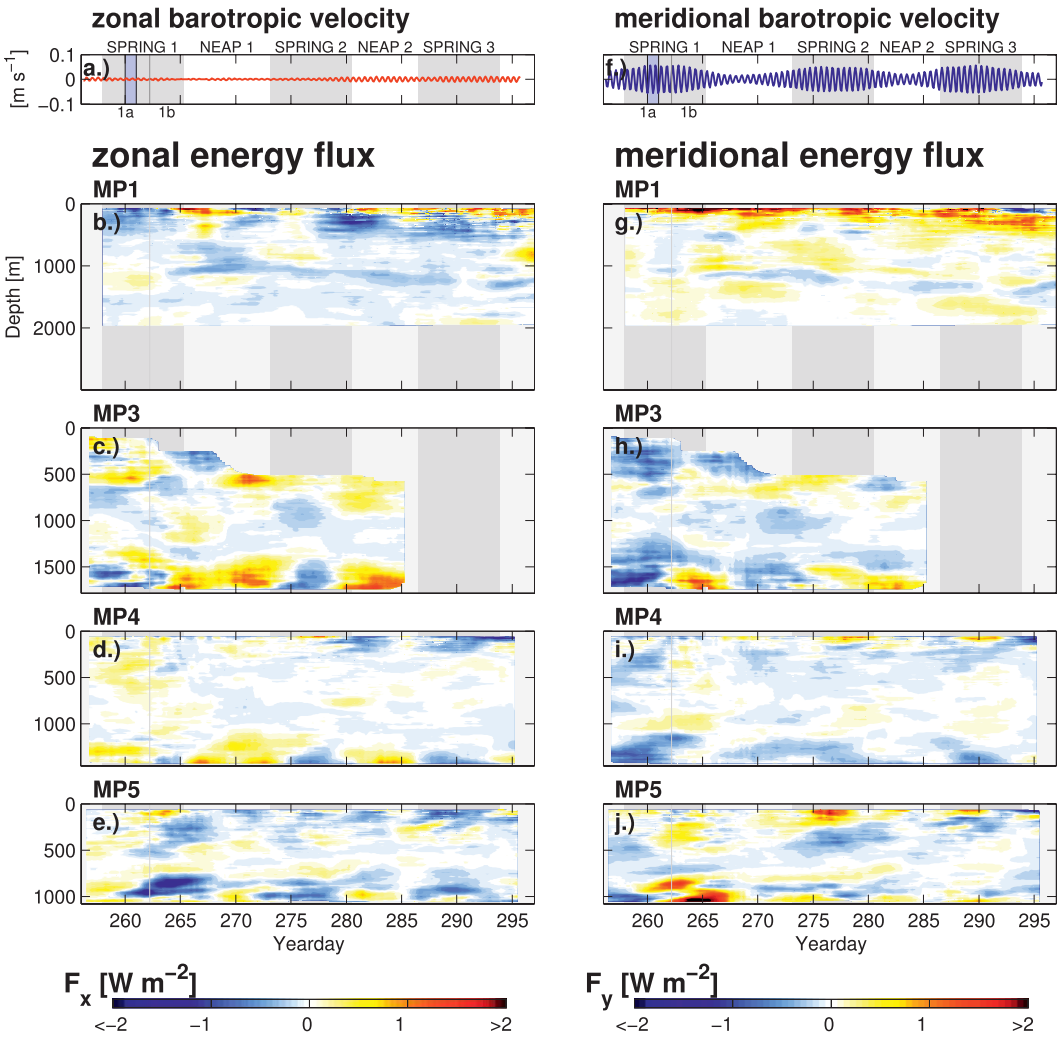

FIG. 6. Semidiurnal barotropic (a) zonal and (f) meridional velocities at MP4. Semidiurnal (b)–(e) zonal and (g)–(j) meridional energy fluxes at MP1–MP5. In (a)–(e), red indicates onshore (eastward) flux and blue indicates offshore (westward) flux. In (f)–(j), red indicates northward flux and blue indicates southward flux. During spring tides 1–3 (gray), strong offshore energy flux is observed within 300 mab at the slope moorings (c)–(e). During local neaps 1 and 2 (white), fluxes within 300 mab are directed onshore.

During each interval, there is significant variability in energy flux, direction, and magnitude. The temporal evolution of horizontal energy flux is shown by the colored vector sticks (Fig. 8). For example, during spring 2, fluxes on the deep slope (MP3 and MP4) are initially onshore (Fig. 8a, red sticks). At the peak of the spring tide (yearday 260), flux rotates offshore (orange), rotating back onshore at the end of spring 2 (yellow).

As noted, energy flux is more complicated during spring 1, where it is both onshore and offshore (Fig. 6). By dividing spring 1 into two intervals, we can more clearly see two distinct internal tide regimes. During spring 1a, flux is predominantly southward and onshore (Fig. 8b), whereas, during spring 1b, it switches to mostly northward and onshore (Fig. 8e). Vertical flux is mostly upward during both springs 1a and 1b (Figs. 9b,e). Average horizontal and vertical slope fluxes on the slope are larger during springs 1a and 1b than in springs 2 and 3.

A 1-day snapshot from contemporaneous XCP and MP data reveals more detail of the complicated flux structure on the slope during spring 1a (Fig. 10). At depths greater than 1000 m (MP3, X3.3, X3.7, MP4, and X4.3), flux is predominantly onshore. Shallower fluxes are both onshore and offshore (MP5, X5.3, X5.7, and MP6). Meridional (alongshore) flux is more complex, having no preferred direction over the bulk of the slope and lacking a common vertical structure. At the offshore

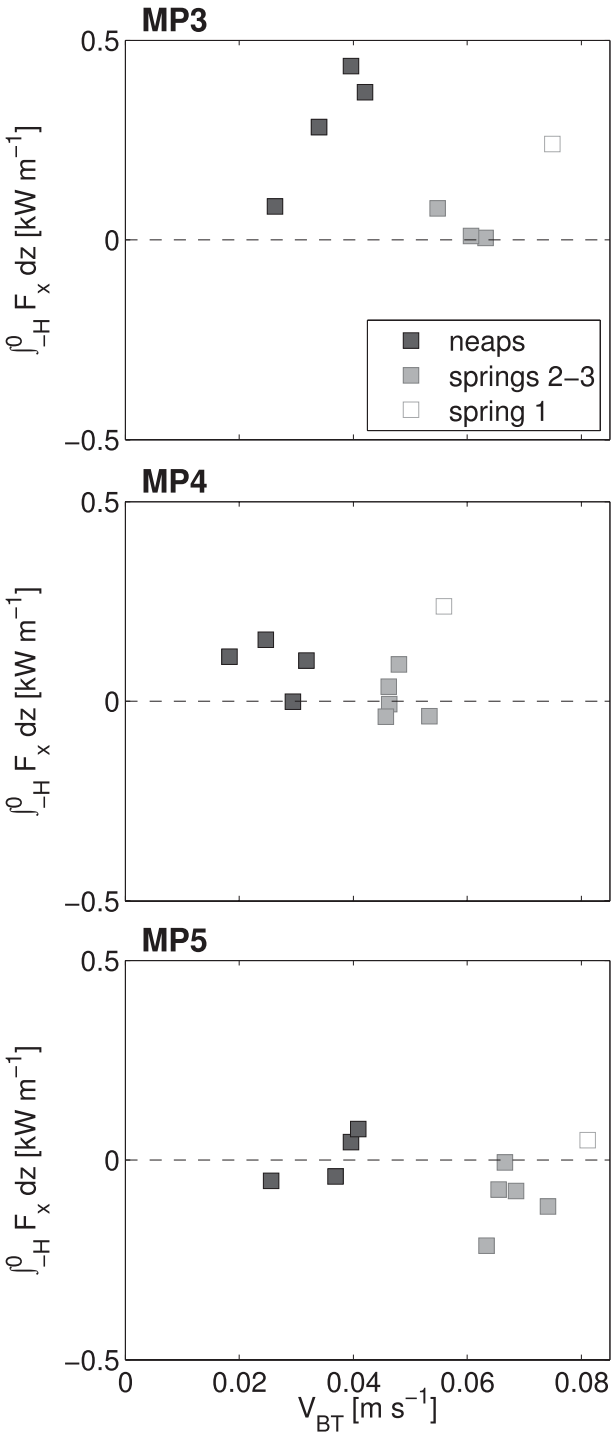

FIG. 7. Scatterplot of barotropic velocity magnitude vs full-depth-integrated zonal fluxes every 3.5 days at slope moorings MP3–MP5 during all neap tides (black squares), the first spring tide (white squares), and the second and third spring tides (gray squares).

mooring (MP1), flux is offshore and northward, in the opposite direction to deep fluxes on the slope.

5. Discussion

a. Local and remote internal tides

The spring–neap cycle of fluxes suggests that the semidiurnal wave field on the Oregon slope must be dominated by two distinct regimes. The first is a locally generated internal tide that radiates offshore and is most clearly observed during spring tides, when local barotropic forcing is strongest. The second is a remotely generated internal tide that shoals onshore and is more likely to overwhelm local signals during neaps, when local barotropic forcing is weaker.

Local generation of internal tides is expected to reach a maximum during spring tides, when barotropic velocities are strongest. Numerical simulations indicate that, when internal tides are generated on the slope, energy flux is directed offshore (S. M. Kelly et al. 2011, unpublished manuscript). During springs 2 and 3, baroclinic velocities and vertical displacements are strong (Fig. 5) and, within 300 mab, mean flux is generally offshore (Fig. 8a,d), consistent with an internal tide generated on the slope. At MP4 and MP5, flux is directed away from a topographic bump to the north and the shelf break, respectively. Both these two topographic features are sources of locally generated internal tides in numerical simulations (S. M. Kelly et al. 2011, unpublished manuscript).

Likewise, local internal tide generation is expected to reach a minimum during neap tides, when barotropic velocities are weakest. However, baroclinic velocities and vertical displacements during neaps 1 and 2 are comparable to those observed during spring tides (Fig. 5). This suggests that, during neaps, the baroclinic signal may be dominated by shoaling internal tides generated at remote locations.

Mean flux at the deepest moorings (MP3 and MP4) is bottom enhanced, onshore, and upslope, consistent with a shoaling internal tide originating offshore. Weaker onshore flux at the shallowest two moorings (MP5 and MP6) may be due to dissipation of the shoaling internal tide before the 1000-m isobath, but the signals are too complex to resolve across-slope differences. Over each neap, meridional flux varies significantly (Fig. 8). These variations are consistent with internal tides from multiple distant sources interacting with a slowly varying offshore eddy field (Rainville and Pinkel 2006b) and possibly interfering with weaker, locally generated waves.

During spring 1a, onshore and offshore fluxes suggest a mixture of both remotely and locally generated internal

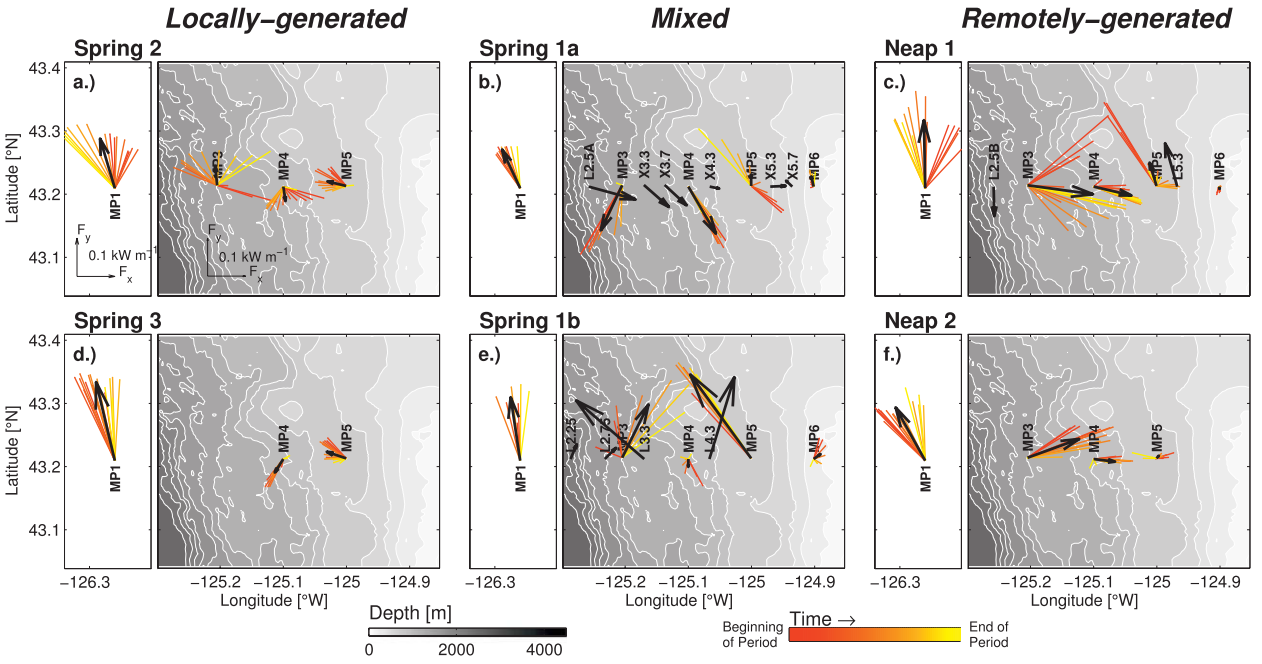

FIG. 8. Local spring tides and neaps are subdivided into periods when (a),(d) local generation; (c),(f) remote generation; or (b),(e) both dominate. Energy flux is depth integrated within 300 mab and averaged over each local spring or neap tide (black arrows). The temporal evolutions of energy fluxes during each local spring and neap tide are plotted at 12-h intervals as colored vector sticks. Vector color indicates the progression of energy flux from the start of each period (red) to the end (yellow). Fluxes in the upper 2000 m at MP1 are shown to the left of each panel. Bathymetry (gray) and 250-m contours (white) on the slope are also shown.

tides. The changing direction from spring 1a to 1b and the strength of energy flux lead us to believe the internal tide during spring 1 is dominated by a time-dependent offshore-generated signal, interfering with a weaker locally generated internal tide. Only at stations extremely close to local sources, such as MP4, do we see similar fluxes during all spring tides (southward and away from the bump to the north).

b. *Superposed internal tides*

Multidirectional wave fields are formed when locally and remotely generated internal tides superpose, such as during spring 1. The resultant interference patterns may lead to the misinterpretation of energy flux and the direction of wave propagation (Nash et al. 2004; Martini et al. 2007). However, by comparing the alignment of energy flux to the semimajor axis of the current ellipse (appendix B), we can determine when internal tides are likely dominated by a single wave (aligned) or a mixture of multiple waves (unaligned). When the wave field is dominated by a single wave (unidirectional), energy flux direction points in the direction of wave propagation. When the wave field is made up of many waves propagating in different directions (multidirectional), energy flux does not necessarily point in the direction of wave propagation. Here, we use this technique to verify whether flux during spring and neap tides represent offshore and onshore propagating internal tides, respectively.

At each mooring, the 100-mab semidiurnal current ellipses and fluxes are plotted in the region where the strongest fluxes are observed (Fig. 11). Internal tides are defined to be unidirectional when flux is aligned within $\pm 35°$ of the semimajor axis, where the ratio of the transverse to the parallel flux is less than f/ω. Circular ellipses are inherently multidirectional and cannot be aligned.

During neaps, aligned flux and ellipse pairs suggest that internal tides are unidirectional at the deep moorings (MP3 and MP4), propagating predominantly onto the slope. Fluxes turn onshore from MP3 to MP4. At MP4, the internal tide propagates nearly perpendicular to the isobaths and observed current ellipses become nearly rectilinear. Ellipses that turn onshore and elongate when moving inshore mimic predictions for reflection of obliquely incident internal waves off a near-critical slope (Eriksen 1982), which will be discussed in section 5d.

At MP4 during spring tides 2 and 3, the internal tide is always directed to the southwest, consistent with local generation at the bathymetric bump located to the northeast. At the midslope moorings (MP4 and MP5) from spring 1a to 1b, there is a switch from a unidirectional

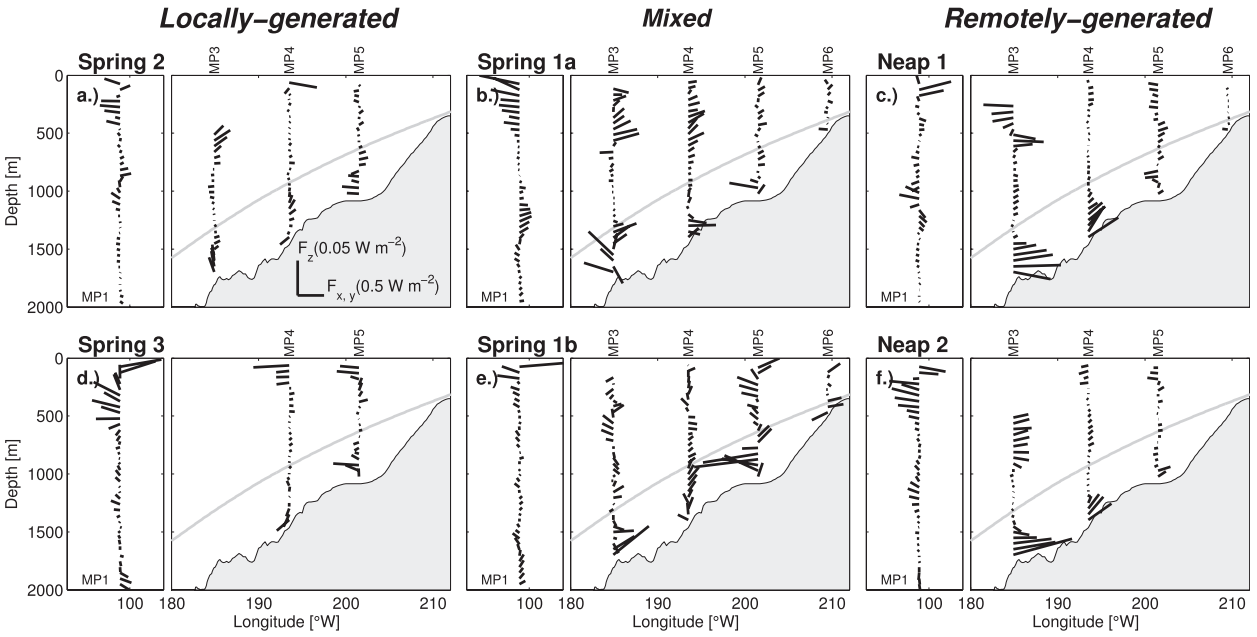

FIG. 9. Mean across-slope vertical energy flux vectors (black sticks) during local spring and neap tides over the slope. Onshore (eastward) zonal flux is to the right, whereas positive vertical flux is upward. Vertical energy flux is nearly an order of magnitude smaller than the zonal energy flux. Their scales are shown in (a). Flux and bathymetry have the same vertical aspect ratio. A semidiurnal characteristic emanating from the shelf break is shown in light gray.

wave field to a multidirectional wave field when the southbound remotely generated internal tide becomes northbound and superposes with the locally generated internal tide. If the local internal tide is generated at the shelf break, we would expect a strong offshore unidirectional wave field at the shallowest mooring (MP6). This is not observed, suggesting a local source closer to MP4 and MP5.

c. *Far-field: Mooring MP1*

The deep mooring, MP1, was designed to capture low-mode tides before they reach the continental slope and are modified through interactions with bathymetry. However, the energy flux on the slope does not appear to have a simple relation to flux at MP1. At the offshore mooring, both low- and high-mode meridional fluxes are always northward, parallel to the continental slope (Figs. 12a,c). Low- and high-mode energy densities (the sum of the potential and kinetic energy) exhibit peaks during both spring and neap tides. High-mode energy density is substantially larger than in low modes, but low-mode flux is larger than in higher-mode fluxes. These observations lead us to hypothesize that the internal tide at MP1 is composed of a quasi-constant northbound remotely generated internal tide that is superposed with a weaker locally generated internal tide with a spring–neap cycle.

Usually, higher modes are associated with local generation because their low group speeds and high shear do not allow them to propagate far from their generation sites before being dissipated. High-mode energy density and fluxes are slightly elevated during the spring tides, suggesting internal tide sources near MP1. Gorda Ridge, a site of abrupt and rough topography 35 km to the southwest of MP1, is one possibility (Fig. 1a). High-mode internal tides from a source farther away than Gorda Ridge may cause meridional flux (Fig. 12c) and energy density (Fig. 12b) to remain high for an additional 3–4 days.

Another high-mode internal tide source might be the Oregon slope itself. Zonal fluxes at MP1 are offshore during neaps (Fig. 12b), roughly when higher modes generated on the slope during spring tide are expected to reach MP1 (mode-5 travel time is ~3.2 days). MP1 high-mode fluxes are similar in magnitude to offshore fluxes generated at MP3 during the local spring (~0.1 kW m^{-1}). Therefore, high-mode internal tides generated on the slope may propagate at least 100 km offshore (past MP1), having undergone one surface reflection with little dissipation or spreading.

Sources south of the array must generate the ~0.3 kW m^{-1} northbound low-mode internal tide observed at the offshore mooring. Mendocino Escarpment (Fig. 1) is one candidate. Althaus et al. (2003) observed the

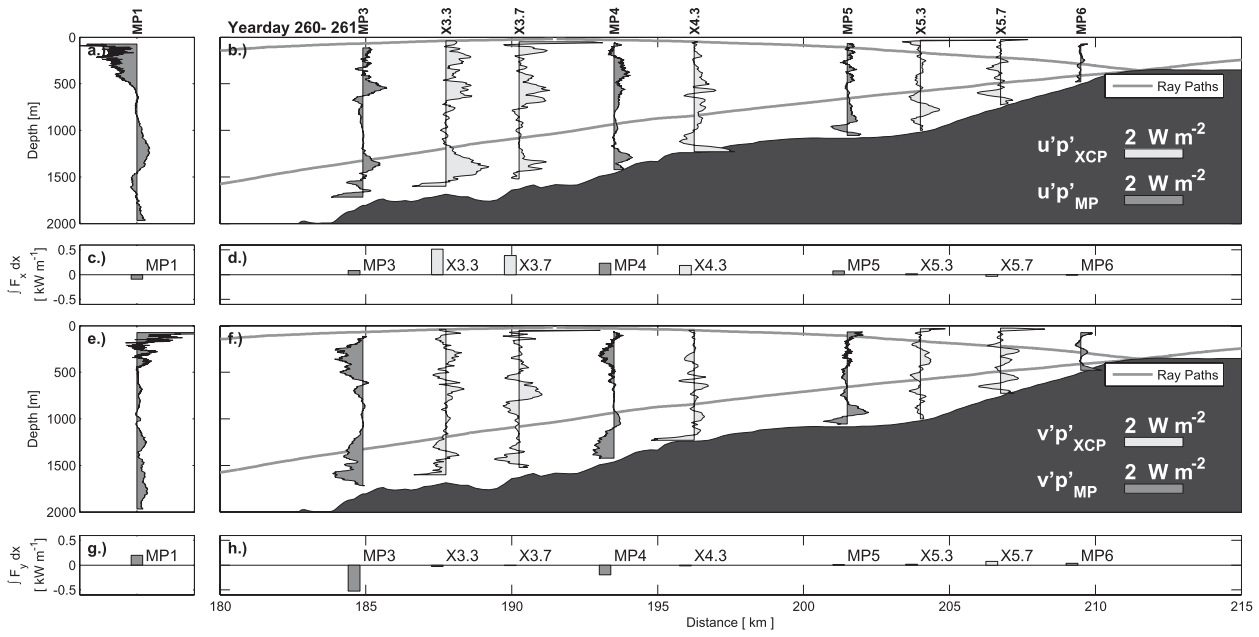

FIG. 10. (a),(b) Zonal semidiurnal energy fluxes during the 18-h XCP from both XCPs (light gray) and MPs (dark gray), where onshore (eastward) fluxes are to the right. (e),(f) Meridional fluxes during the same time period, where northward and southward energy fluxes are directed to the right and left, respectively. (c),(d) Depth-integrated zonal energy fluxes. Positive values indicate onshore (eastward) flux. (g),(h) Depth-integrated meridional energy fluxes. Positive values indicate northward flux. Semidiurnal characteristics emanating from the shelfbreak are plotted in light gray.

generation of a 4 kW m^{-1} northward-propagating internal tide at Mendocino, reducing to 2 kW m^{-1} after the first surface reflection. To find when internal tides generated at these sites arrive at the moored array, mode-1 travel times are computed using depth and mean stratification along the propagation path following Rainville and Pinkel (2006b). If the low-mode signal at MP1 was only generated at Mendocino, one would expect a mode-1 spring–neap cycle lagging the local cycle by 2.3 days, the mode-1 travel time from Mendocino to MP1. Low-mode energy flux and density lack a distinct lagged spring–neap cycle, implicating other sources.

In addition to high modes, Gorda Ridge and the continental slope might also generate the observed low modes. Mode-1 internal tides from Gorda Ridge and the continental slope arrive at MP1 approximately 6 and 17 h after being generated, respectively. This small difference in travel time makes it difficult to isolate low-mode tides originating from these two sources, whose spring–neap cycles are nearly indistinguishable.

d. Shoaling internal tides

During neaps, onshore-propagating internal tides are bottom intensified, qualitatively agreeing with predictions for shoaling internal waves (Wunsch 1968, 1969) or near-critical reflection (Eriksen 1982). In addition, bottom-intensified fluxes appear to turn onshore as they shoal, also as predicted for oblique (nonnormal) reflection. At the deepest slope mooring MP3, fluxes are to the northeast. Moving upslope to MP4, fluxes rotate to the east. However, there is no corresponding onshore flux at the offshore mooring (MP1), implying the northbound internal tide must be turned onshore if linked to the shoaling internal tide. Here, we examine whether near-critical reflection from the slope directs the northbound internal tide onto the slope.

The bulk of the Oregon slope is supercritical or near critical with respect to the semidiurnal tide. Slope criticality is determined by comparing the bathymetric slope ($s = \nabla H$) to the slope of the internal tide characteristic when it intersects the bottom,

$$\alpha = \sqrt{\frac{N^2 - \omega_{M_2}^2}{\omega_{M_2}^2 - f^2}}, \tag{9}$$

where N is the stratification at the seafloor. Bathymetric slopes are supercritical (subcritical) when steeper (gentler) than the slope of the semidiurnal characteristic. When the bathymetric slope is supercritical (subcritical), an incident internal tide propagating onshore normal to the slope will reflect offshore (onshore).

To compare our observations to theory, we have constructed a simple analytical model of an obliquely

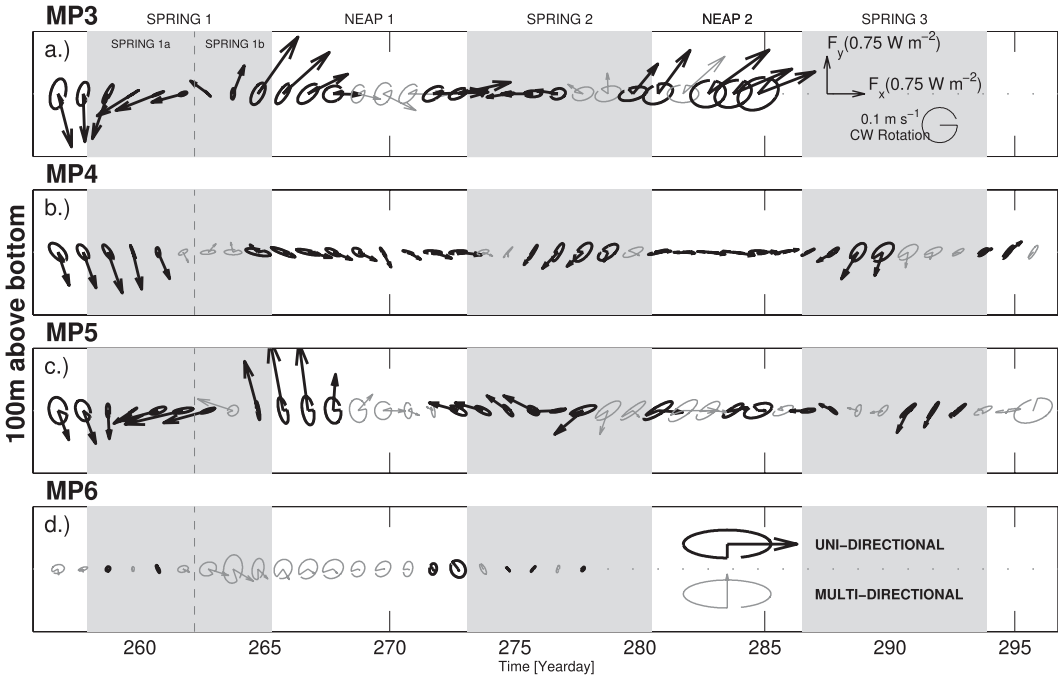

FIG. 11. Daily semidiurnal current ellipses and energy fluxes at 100 m above the bottom on the slope (MP3–MP6). The internal tide is unidirectional when the ellipses and fluxes are aligned to within 35° (black) and multidirectional when they are not (gray). (bottom) Examples of both uni- and multidirectional ellipse–flux pairings are shown, with both having clockwise current vector rotation. Ellipses and fluxes are oriented such that eastward (upslope) velocity is to the right and northward (along slope) velocity is upward.

incident mode-1 internal tide shoaling onto a supercritical slope following Eriksen (1982, 1985). Internal tides shoaling onto a subcritical slope would also be turned onshore. However, the majority of the slope is supercritical (>70%), making it unlikely that shoaling internal tides are turned onshore by subcritical reflection.

From vertical velocity, $w = A_i e^{i(k_i x + l_i y + m_i z - \omega t)} + A_r e^{i(k_r x + l_r y + m_r z - \omega t)}$, the incident and reflected internal tidal velocities, vertical displacements, and pressure perturbations are solved for using equations from Eriksen (1982), section 2, and the internal wave polarization equations. The slope is a wedge, infinitely long in the meridional direction (Fig. 13). Stratification is constant ($N = 2.4 \times 10^{-3}$ s^{-1}). The incident azimuthal angle is $\theta_i = \tan^{-1}(l_i/k_i)$, a function of the incident across- and along-slope horizontal wavenumbers k_i and l_i, respectively. The incident mode-1 internal tide is a vertically standing wave, constructed from upward- and downward-propagating waves whose wavelengths are twice the abyssal depth (mode-1 $\lambda_z = 2H \sim 2 \times 2800$ m).

In the case of normally incident supercritical reflection (i.e., two dimensional and $\theta_i = 0°$), both the upward- and downward-propagating components of the incident mode-1 wave reflect from the slope directly offshore ($\theta_r = 180°$) to lower and higher vertical wavenumber m_r, respectively (Fig. 13, left). In contrast, at large azimuthal angles ($\theta_i \to 90°$), the upward component is initially reflected from the surface, because its slope is steeper than the bathymetric slope over which it travels (Fig. 13, right, red), and is then reflected from the slope offshore to high wavenumber. As the azimuthal angle decreases (approaching the normal case), the bathymetric slope over which the upward component travels becomes steeper. Eventually, the wave slope is no longer larger than the bathymetric slope. Then the incident upward component once again intersects the slope and is reflected onshore and upward, similar to the normal case. For all incident azimuthal angles, the downward component is always reflected offshore to higher vertical and across-slope wavenumber (blue).

Energy density and flux from the idealized model are shown in Fig. 14 and compared to neap tide observations at yearday 269.4 in Fig. 15. The modeled incident mode-1 wave has the same depth-integrated horizontal flux magnitude (F = 533 W m^{-1}) and azimuthal incidence (θ_i = 82°) as the mode-1 tide observed at MP1 (Fig. 14a). To compare to the idealized model, MMP observations are Wentzel–Kramers–Brillouin (WKB) scaled to simulate an ocean with constant stratification (Leaman and Sanford 1976). The depth coordinate is stretched to $z_{\mathrm{wkb}} = \int_z^0 (\overline{N}(z)/N_0)\, dz'$, and horizontal energy flux and density are scaled by $(E_{\mathrm{wkb}}, F_{\mathrm{wkb}}) = (E, F)N_0/\overline{N}(z)$.

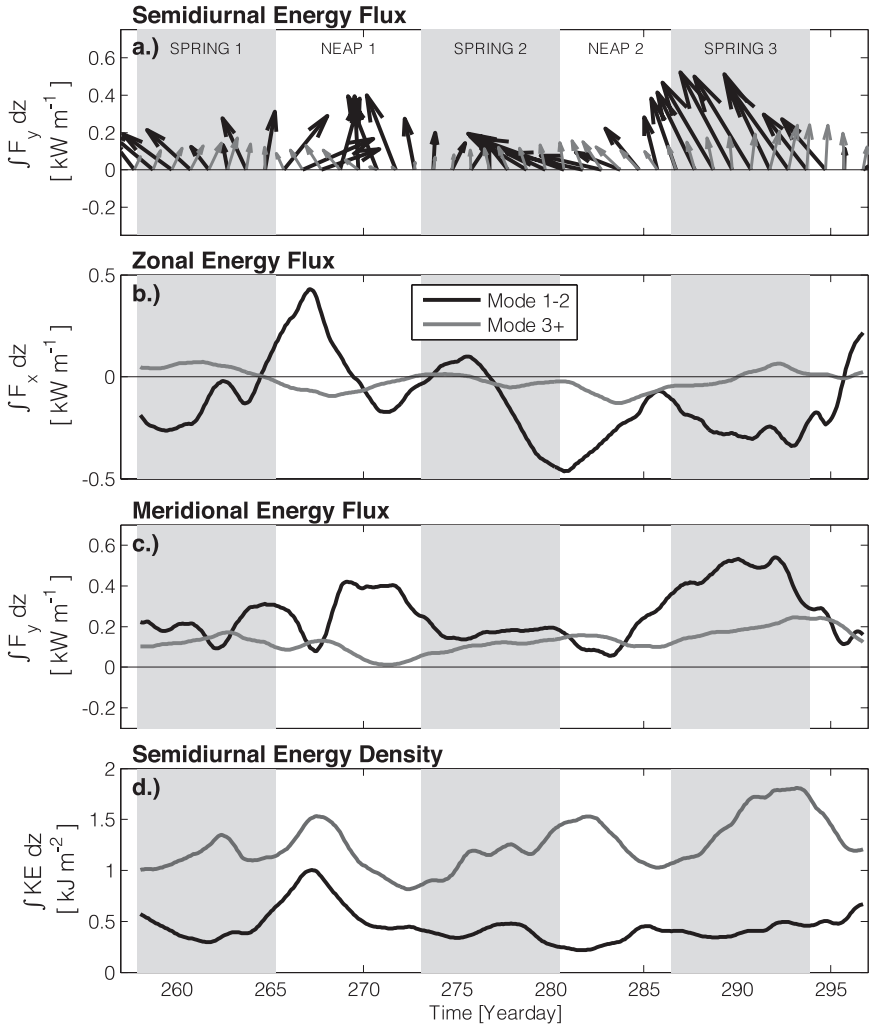

FIG. 12. Depth-integrated energy flux and density at the offshore mooring MP1. (a) Plan-view vector time series of low- (black) and high-mode (gray) semidiurnal flux at 12-h intervals. Onshore (eastward) fluxes are to the right, and northward fluxes are to the top of the page. (b) Zonal and (c) meridional fluxes are presented separately. (d) Energy density is the sum of potential and kinetic energy. In all panels, low-mode values are the sum of mode 1 and mode 2 integrated over the full depth (2995 m). High mode contains modes 3 and above and are obtained by depth integrating each value over the upper 2000 m once the low modes have been removed.

Similar to observations on Fieberling Guyot (Eriksen 1998), downward waves reflected from near-critical slopes probably do not propagate far from the bottom after reflection, dissipating because of their large amplitudes, shear, and vertical wavenumber. To simulate near-bottom dissipation after reflection, a vertical damping function, $A_r(z) = \exp[-(z/1000)^2]$, where A_r is the reflected wave amplitude, is applied. Without the damping function, energy and fluxes above 500 mab in the idealized model would be similar in magnitude to near-bottom values, inconsistent with observed fluxes. Dissipation of reflected internal tides may account for the enhanced turbulence observed by Moum et al. (2002) and Nash et al. (2007).

Model results and WKB-stretched observational data are similar at most of the moorings (Fig. 15). Modeled zonal energy fluxes and densities are bottom intensified and are of similar magnitude to observations. Energy flux direction is similar in both the model and observations. However, the model predicts strong northward fluxes near the surface, which are not observed in the data.

Because the bathymetric slope is so close to critical, the model is highly sensitive to changes in slope steepness. For all incident azimuthal angles in the idealized

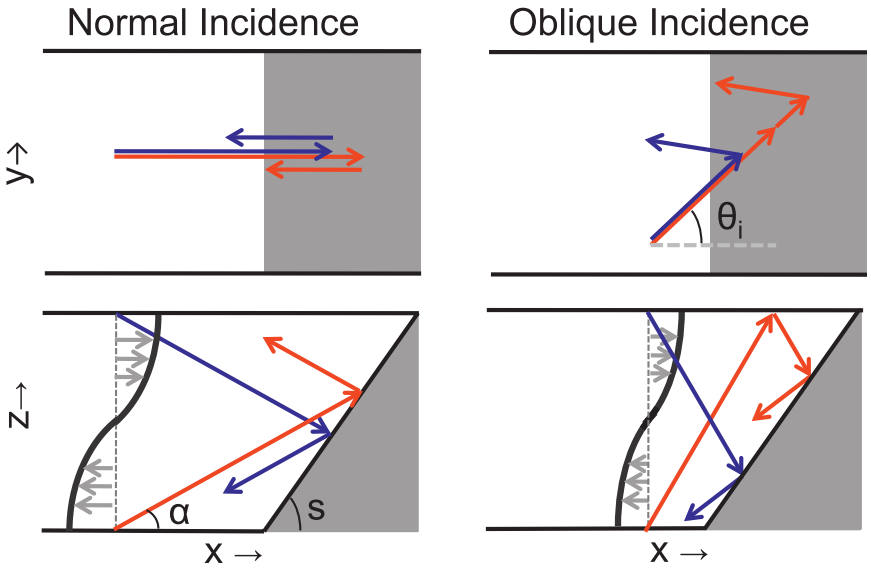

FIG. 13. Diagrams of (left) normally and (right) obliquely incident mode-1 tides reflecting from a supercritical slope in constant stratification. A mode-1 wave (black line, gray arrows) is modeled as a vertically standing wave created by the superposition of upward (red) and downward (blue) propagating waves. In the normal case, the bathymetric slope is steeper than the ray slope and both the upward and downward beams reflect from the slope. In the oblique case, the slope of the upward wave is steeper than the bathymetric slope over which it travels and the upward beam only intersects the slope after reflection downward from the surface. The superposition of the incident and reflected waves in the oblique case leads to onshore energy flux.

supercritical model, when the bathymetric slope becomes gentler and approaches the semidiurnal critical slope, $\alpha = 0.041$, the amplitude and vertical wavenumber of the downward wave reflected from the slope increase dramatically (Table 1, m_r^{down}). Therefore, the modeled internal tide is dominated by the initially downward-reflected ray and is predominantly offshore, downward (contrary to observed neap fluxes), and high wavenumber, unlike shoaling internal tides observed during neaps. However, what is observed is the superposition of the incident low-wavenumber and reflected high-wavenumber tides. They produce a complex flux interference pattern, resulting in onshore and offshore fluxes that switch direction over very small vertical scales (<200 m), similar to those observed during the XCP survey (Fig. 10). The interference pattern can be shifted vertically and to higher wavenumber as the slope changes but will always produce both onshore and offshore fluxes.

Simple models such as the one presented here can aid interpretation of complex internal tide observations on a slope. However, our model does not take into account bottom roughness or stratification changes that affect criticality and characteristics of the reflected internal tide. Because the bathymetric slope is so close to critical and changes across the slope, it is difficult to tune the model to exactly match the observations at all moorings. Additionally, the simple slope model does not include horizontal flux convergence (Nash et al. 2007) or a multidirectional incident internal tide (i.e., from multiple sources). However, the similarity of modeled to observed energy flux and density suggests the northbound low-mode internal tide is indeed turned onshore by near-critical reflection from large-scale bathymetry.

6. Conclusions

On the Oregon continental slope, the content and direction of the internal tide changes both spatially and temporally over the 40-day observational period. Observations from a moored array support the presence of two dominant internal tide components: (i) internal tides generated on the slope that propagate offshore and are observed during local spring tides and (ii) internal tides that shoal onshore and are exposed during weak local neaps. The wave field on the slope is complex because of superposition of these remote and local internal tides as well as incident and bottom-reflected waves, making interpretation challenging. By identifying when internal tides are unidirectional, we can partially disentangle a wave field that is often made up of internal tides from multiple local and remote sources. These

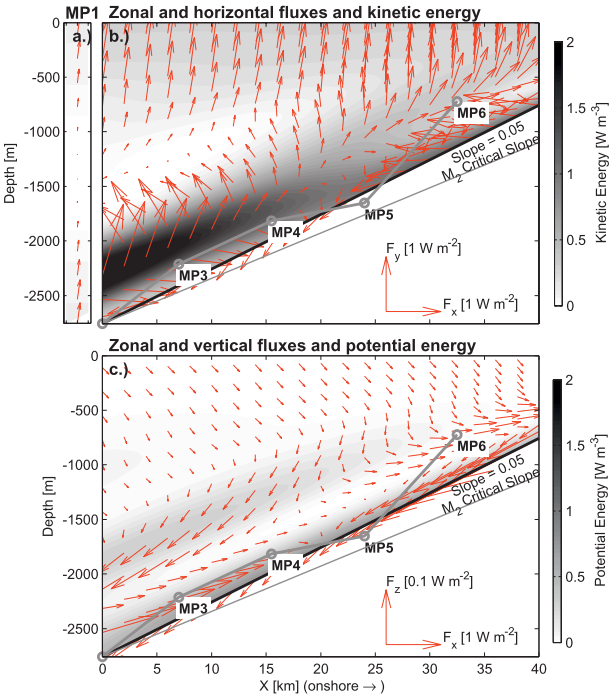

FIG. 14. (a) Idealized model of a mode-1 internal tide obliquely incident on a supercritical wedge with constant stratification. Incident mode-1 horizontal flux magnitude and direction are identical to the mode-1 tide observed at the offshore mooring (MP1) at yearday 269.4 during neap 1. (b) Zonal and meridional energy fluxes (red arrows) and kinetic energy (shading). (c) Zonal and vertical energy flux (red arrows) and potential energy (shading). WKB-stretched mooring depths (gray circles), the mean slopes between them (thick gray lines), and the semidiurnal critical slope (thin gray line) are shown in (a)–(c).

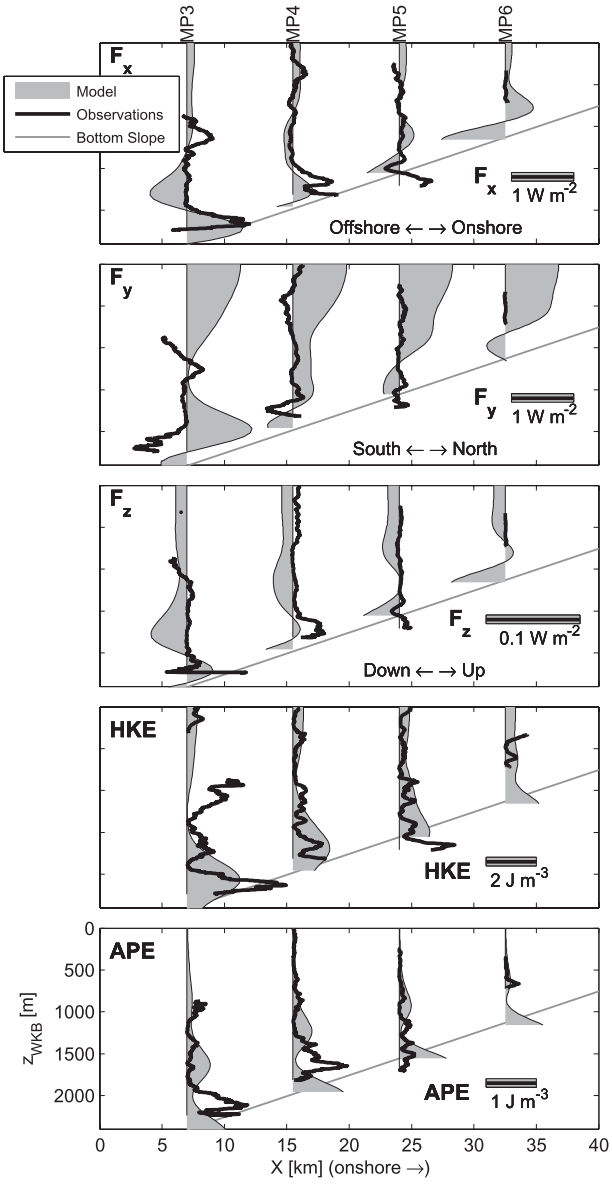

FIG. 15. (top)–(bottom) Zonal flux, meridional flux, vertical flux, horizontal kinetic energy, and available potential energy from the idealized supercritical slope model (gray patch) compared to WKB-scaled MP data (black line) during neap 1 at yearday 269.4.

techniques might be useful in diagnosing multidirectional internal tides and the direction of internal tide propagation at other locations similar to the Oregon slope, where there is a time-varying internal tide. Observations at a mooring 100 km offshore (MP1) suggest that the remotely generated internal tide predominantly originates south of the array. By comparing our observations during neap tide to a simple model of internal tide reflection on a slope, we show that, when the northbound internal tide observed at MP1 impinges upon the slope, it undergoes near-critical reflection and turns onshore.

Locally generated internal tides are produced by flow over small-scale bathymetry on the slope (S. M. Kelly et al. 2011, unpublished manuscript). During spring tides, these can overwhelm the shoaling of remote waves, leading to a net offshore energy flux. High modes generated on the slope are expected to dissipate locally and not propagate far offshore because of their low group speeds and high shear. However, our observations at MP1 suggest a portion of the weak, high-mode internal tide is able to escape the slope to the offshore mooring MP1. Relatively smooth bathymetry between the Oregon slope and offshore mooring provides little opportunity for dissipation because of reflection or scattering, possibly allowing the high-mode internal tide to propagate over 100 km offshore. Slowly propagating high-mode internal tides may persist until interacting with other offshore features, such as seamounts, submarine ridges, or the mesoscale eddy field.

On the Oregon slope, the remotely generated internal tide does not exhibit a spring–neap cycle. The abundance of

TABLE 1. In the first line are the initial parameters used in the supercritical slope model (s, α, m_i, θ_i) and outputs: reflected vertical wavenumber m_r, azimuthal direction of the reflected component θ_r, and the surface each component is reflected from. The bathymetric slope is then changed from a large incident angle ($\theta_i = 82°$) to a more moderate incident angle ($\theta_i = 45°$). Finally, the azimuthal angle of incidence is varied, whereas the bathymetric slope is held constant.

Incident rays				Upward ray			Downward ray		
s	α	m_i	θ_i	m_r^{up}	θ_r^{up}	Reflects from	m_r^{down}	θ_r^{down}	Reflects from
0.05	±0.041	±0.0011	82°	0.0011	82°	Surface	0.0070	171°	Slope
0.2	±0.041	±0.0011	82°	0.0011	82°	Surface	0.0013	121°	Slope
0.055				0.0011	82°	Surface	0.0047	166°	Slope
0.045				0.0011	82°	Surface	0.016	176°	Slope
0.2	±0.041	±0.0011	45°	−0.0009	116°	Slope	0.0029	16.4°	Slope
0.059				−0.0011	45.8°	Slope	0.0056	172°	Slope
0.055				0.0011	45°	Surface	0.0069	173°	Slope
0.045				0.0011	45°	Surface	0.024	178°	Slope
0.05	±0.041	±0.0011	0°	−0.00011	180°	Slope	0.012	180°	Slope
			33°	−0.0011	35°	Slope	0.011	177°	Slope
			34°	0.0011	34°	Surface	0.011	177°	Slope
			90°	0.0011	90°	Surface	0.0061	169°	Slope

offshore sources—Mendocino Escarpment, Gorda Ridge, and the Juan de Fuca Ridge—and refraction through the mesoscale eddy field (Rainville and Pinkel 2006b) may all contribute to intermittency of these shoaling internal tides. Meandering northbound internal tides generated at Mendocino Escarpment may turn onshore or offshore, changing the latitude at which they first impinge upon the continental slope; if turned offshore, the low-mode internal tide may never reach the Oregon slope. The situation is complicated by a wave field composed of internal tides from many sources, each intersecting the slope at different locations and times. Whether propagating internal tides are directed onto features on which they will dissipate may account for the heterogeneity and intermittency of turbulence on the continental slope observed by Nash et al. (2007). The Oregon continental slope is a site where remotely generated internal tides dissipate, as demonstrated by observations of steepening and the formation of upslope bores, which lead to enhanced mixing over the slope (K. I. Martini et al. 2011, unpublished manuscript).

The two-dimensional description provided by the moored array is inadequate to fully characterize the propagation of remotely generated internal tides onto the Oregon slope; a three-dimensional picture is needed. Our idealized three-dimensional model suggests that large-scale bathymetry guides obliquely incident internal tides onto the slope, rather than reflecting them offshore (as in the two-dimensional model). However, this model is unable to address the effects of small-scale bathymetry, including changes in criticality across the slope and dissipation due to bathymetric roughness. Though further observations and modeling are required, our results suggest that near-critical reflection of obliquely incident internal tides onto continental slopes may be a key mechanism for dissipating deep-ocean internal tides.

Acknowledgments. This work was supported by National Science Foundation Grants OCE-0350543 and OCE-0350647. The authors thank Charlie Eriksen for helpful discussions about this work. We would also like to thank Dicky Allison, Eric Boget, Andrew Cookson, Kevin Bartlett, Richard Dewey, Eleanor Frajka-Williams, Dave Winkel, Zhongxiang Zhao, and the captain and crew of the R/V *Wecoma* for their technical and at-sea expertise.

APPENDIX A

Resolving the Baroclinic Internal Tide

The sawtooth sampling pattern of the MMP results in temporally inhomogeneous resolution (3 h at the top and bottom and 1.5 h at middepth), giving rise to the possibility of spatial/temporal aliasing. To ascertain whether the semidiurnal internal tide can be accurately obtained from MMP data, two sensitivity studies are conducted. In the first, we determine the effect of aliasing of baroclinic motions onto barotropic velocity estimates. In the second, we determine how surface gaps and temporal aliasing of the baroclinic velocity affect the calculation of energy flux.

a. Barotropic tide

Observed barotropic current ellipses have larger zonal velocities and are rotated from TOPEX/Poseidon global tidal model (TPXO) predictions (Egbert and Erofeeva 2002). These differences are largest at the deepest slope mooring, MP3, where the observed ellipse is rotated as much as 31° clockwise from TPXO. Predicted meridional barotropic velocities (~0.037 and ~0.014 m s^{-1} during spring and neap, respectively) are comparable and in

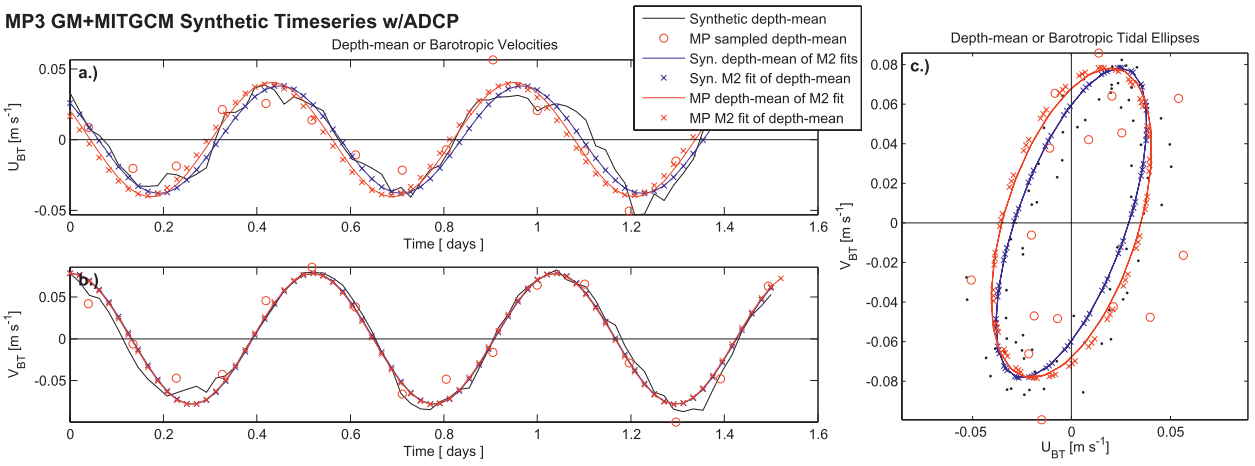

FIG. A1. Comparison of semidiurnal barotropic velocities from a synthetic GM plus semidiurnal wave field at MP3 (blue) and the same wave field sampled by a moored profiler (red). Shown are (a) zonal barotropic velocities, (b) meridional barotropic velocities, and (c) barotropic current ellipses. In (a)–(c), the true total (black lines or dots) and semidiurnal barotropic velocities (blue lines and hatches) are compared to total (red circles) and semidiurnal barotropic velocities (red lines and hatches) obtained when sampling the same synthetic wave field with a moored profiler. The semidiurnal barotropic velocity is most accurately obtained by taking the depth mean of the semidiurnal fits at each depth (red lines).

phase with observations (~0.043 and ~0.015 m s^{-1}). However, in the zonal direction, barotropic velocities can be 0.01–0.03 m s^{-1} larger than TPXO predictions and often 120° out of phase. If not sampled adequately, stronger zonal baroclinic velocities (<0.2 m s^{-1}) can be aliased onto weaker zonal barotropic velocities (<0.025 m s^{-1}). Using a synthetic wave field subsampled as an MMP in a sawtooth pattern, we demonstrate that these differences are not due to aliasing but are real variations in the direction and phasing of the barotropic tide due to small-scale bathymetry not resolved in global tidal models, not unreasonable over complex bathymetry.

For this aliasing study, a 1.5-day velocity depth/time series is constructed by combining a synthetic Garrett–Munk (GM) wave field with semidiurnal output from a tidally forced Massachusetts Institute of Technology general circulation model (MITgcm) of the Oregon slope (S. M. Kelly et al. 2011, unpublished manuscript). MITgcm is a nonlinear, nonhydrostatic, z-coordinate, implicit free-surface, finite-volume model (Marshall et al. 1997). Baroclinic and barotropic velocity magnitudes from MITgcm are scaled to match observations. The synthetic wave field is subsampled as an MMP in the interior and as an ADCP in the upper 50 m. Then, harmonic analysis was used to extract the M_2 signal at each depth level from the fully sampled and MMP/ADCP-sampled synthetic time series.

For both sampling schemes, barotropic velocities are computed using three different methods: (i) the depth mean of each velocity profile, (ii) the depth mean of the M_2 fits, and (iii) the M_2 fit to the depth mean of the each velocity profile. One realization of the synthetic barotropic semidiurnal spring tide is shown in Fig. A1. Profile depth means (red circles) do not accurately represent the true barotropic velocity (black). However, the true M_2 barotropic velocity (blue) is well described by both the depth mean of the M_2 fits (red line) and the semidiurnal fits to the depth mean (red crosses). Errors for the MMP/ADCP-sampled M_2 zonal and meridional velocity amplitudes are 3.4% and <0.1%, respectively. Phase is offset from true zonal and meridional values by 18° and 2°, respectively. The MMP/ADCP-sampled ellipse is slimmer and rotated several degrees counterclockwise relative to the ''true'' barotropic ellipse. Overall, the effect of baroclinic aliasing is negligible, and the depth mean of the semidiurnal fits adequately reproduces the true M_2 spring tides. We conclude that differences between observations and TPXO are likely the result of small-scale bathymetry not resolved in the tidal model.

Baroclinic aliasing is larger when barotropic velocities are smaller (i.e., during neaps). Zonal barotropic velocities are most strongly affected (~34% error and ±36° phase offset) because they are an order of magnitude smaller than the baroclinic velocities. Aliasing is much smaller for meridional barotropic velocities (~4% error and ±7° phase offset).

b. *Energy flux*

1) SURFACE GAPS

After 10 days, the MMP at MP3 stopped profiling the upper 500 m of the water column. Data gaps near the surface affect whether semidiurnal energy fluxes ($u'p'$)

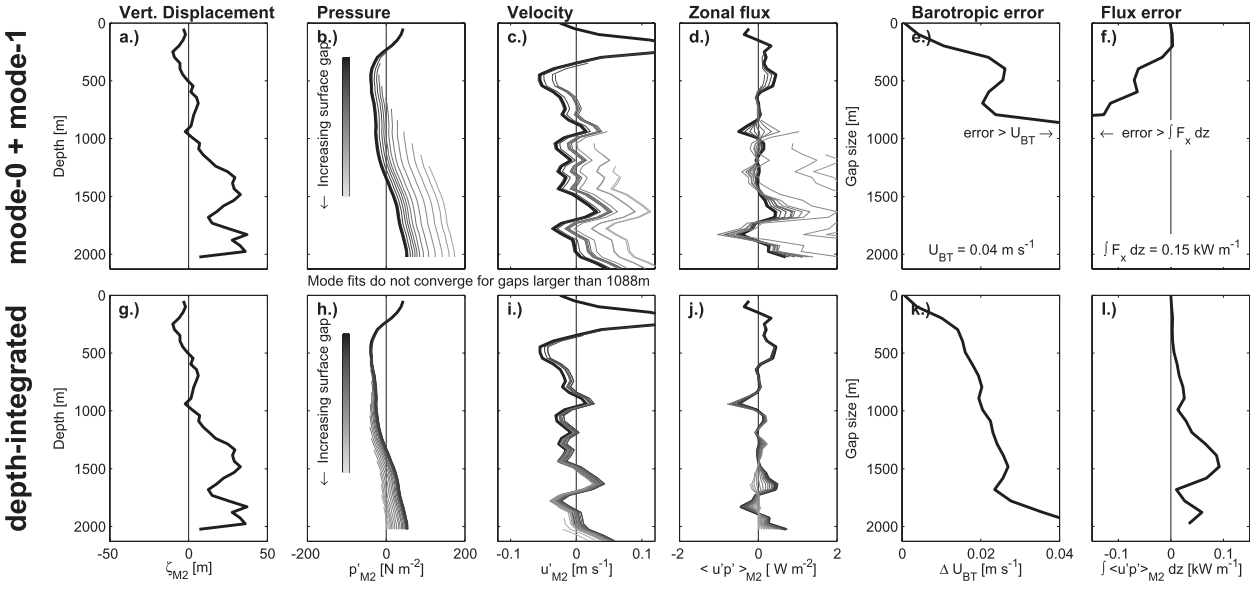

FIG. A2. Effect of increasing surface gaps on accuracy when finding the semidiurnal pressure perturbation, baroclinic velocity, and energy flux from a 24-h LADCP/CTD survey (L2.5a). For both the pressure and velocity, the baroclinicity condition is satisfied by removing either (a)–(f) the mode-0 fit or (g)–(i) the depth-mean value. From (a),(g) a single vertical displacement profile, (b),(h) the true, full-depth pressure profile is found (thick black line). (b),(h) As the surface gap becomes larger in a truncated vertical displacement profile, pressure is increasingly offset (gray lines). (c),(i) A similar effect is seen in the baroclinic velocity (gray lines) because of (e),(k) increased barotropic velocity error with increased gap size. Errors due to surface gaps propagates to both (d),(j) the energy flux profile and (f),(l) depth-integrated energy flux, both averaged over a wave period. For surface gaps larger than 1100 m (~50% of the water column), modal regression becomes unstable. Removing the depth mean most accurately reproduces the true pressure, velocity, and energy flux profiles.

at MP3 can be accurately determined from velocity and vertical displacement data. Unlike Nash et al. (2005), here we use LADCP/CTD observations at L2.5a during the spring tide (Fig. A2), which span the full water column, rather than a synthesized internal wave field. We show that surface gaps smaller than 600 m (or ~30% of the water column) are tolerable for our dataset, where energy flux can be found to within 10% of the true value.

Baroclinic velocity u' is found by removing the barotropic or depth-mean velocity U_{BT} to satisfy the baroclinicity condition. In a similar manner, baroclinic pressure perturbation p' is calculated by vertically integrating the vertical displacement scaled by the stratification $\rho_0 N^2 \zeta(z)$ from the surface downward and then removing the depth mean $\overline{p'}$ to satisfy the baroclinicity condition.

Surface gaps, such as those at MP3, affect our ability to correctly determine $\overline{p'}$ and U_{BT}. We use two different techniques to solve for both. First, $\overline{p'}$ and U_{BT} are defined as the depth mean of the truncated profiles. Second, $\overline{p'}$ and U_{BT} are found by linearly regressing a constant (mode 0) plus the first baroclinic mode onto $\rho_0 \int_z^0 -N^2 \zeta(z)\, dz$ and $\int_z^0 u(z)\, dz$, respectively, following Rainville and Pinkel (2006a), where mode 0 is the solution for $\overline{p'}$ and U_{BT}. Nash et al. (2005) regress onto additional, higher modes to reduce the error when the surface gap is small. Here, regression onto just one additional mode, mode 2, introduces large errors in $\overline{p'}$, so it is not used here.

Energy fluxes averaged over a semidiurnal wave period (Figs. A2d,j) are found from 167 nearly full-depth vertical displacement (Figs. A2a,g) and velocity (Figs. A2c,i) profiles. Individual profiles (black line) are truncated at 100-m intervals from the surface downward to simulate increasing surface gaps (gray lines). For either method, gaps less than 660 m produce p' and u' offsets less than 50 N m^{-2} and 2.6 cm s^{-1}, respectively. For larger gaps (>600 m), offsets increase. Offsets are largest when using modal fits. Offsets in u' are caused by errors in U_{BT} (Figs. A2e,k), which increase with surface gap size. Similarly, energy flux error (calculated here as the difference between the full-depth and truncated depth-integrated energy fluxes) is small for gaps <600 m, increasing with larger gaps (Figs. A2f,l).

When there are large surface gaps, using depth integration to find $\overline{p'}$ and U_{BT} is the most robust method to calculate energy fluxes on the Oregon continental slope. When employing modal regression, regression onto unrealistic modal solutions, such as flat-bottom modes on a slope, gives incorrect values for $\overline{p'}$ and U_{BT},

especially when there are surface gaps. Therefore, to minimize error when calculating energy flux, depth-integrated values for p' and U_{BT} should be used (Kelly et al. 2010). At MP3, where the surface gaps are largest (~500 m), flux errors are <0.5 W m^{-2} and do not appreciably change the direction or magnitude of observed energy flux profiles. For gaps less than 500 m, depth-integrated flux error is <0.01 kW m^{-1}, less than 5% of the true value. If surface gaps are larger than 1000 m, depth-integrated flux errors become greater than 20%.

2) Baroclinic aliasing

In addition to affecting barotropic tidal estimates, aliasing of the baroclinic internal tide onto the barotropic tide can also be another source of error when calculating energy flux. If the barotropic velocity $U_{BT}(t)$ is aliased and therefore incorrect, removing it from the total velocity $u(z, t)$ can result in incorrect baroclinic velocities $u'(z, t)$ and subsequently energy flux $u'p'$. The sensitivity of energy flux to removing an incorrect barotropic velocity is determined by removing four different barotropic velocities: 1) depth mean; 2) $M_2 + S_2$ fit to depth mean over the entire time series; 3) TPXO predictions; and 4) $U_{BT} = 0$, to find the baroclinic velocity at MP3. No matter which barotropic velocity was removed, depth-integrated energy flux averaged over a wave period differed by <0.01 kW m^{-1}, less than 10% of the true value. Therefore, the effect of baroclinic aliasing on depth-integrated energy flux is negligible. For individual profiles, the effect can be larger. In the meridional direction, where barotropic velocities are the largest, energy flux can vary up to 1.2 W m^{-2}, depending on which barotropic velocity is removed. However, on average they are 0.12 W m^{-2}, significantly smaller than observed fluxes.

APPENDIX B

Uni- and Multidirectional Wave Fields

When locally and remotely generated internal tides superpose, they create a multidirectional wave field. Describing a multidirectional wave field (as during spring 1b) can be difficult, because the direction of energy flux does not always correspond to the direction of wave propagation.

To decipher the complex internal tide on the slope, we identify when the internal tide is likely to be unidirectional so flux will indicate the direction of internal tide propagation. The polarization equations for two internal tides with different horizontal and vertical wavenumbers propagating in the same horizontal direction are

$$u' = u_1 \cos(k_1 x + m_1 z - \omega t) + u_2 \cos(k_2 x + m_2 z - \omega t), \tag{B1}$$

$$v' = -u_1 \frac{f}{\omega} \sin(k_1 x + m_1 z - \omega t) - u_2 \frac{f}{\omega} \sin(k_2 x + m_2 z - \omega t), \quad \text{and} \tag{B2}$$

$$p' = u_1 \frac{\omega^2 - f^2}{\omega k_1} \cos(k_1 x + m_1 z - \omega t) + u_2 \frac{\omega^2 - f^2}{\omega k_2} \cos(k_2 x + m_2 z - \omega t), \tag{B3}$$

where k_1 and k_2 are the horizontal wavenumbers along the axis of propagation and m_1 and m_2 are the vertical wavenumbers. In a unidirectional wave field, the semimajor axis of the baroclinic current ellipse is aligned along the axis of propagation and the ratio of the semiminor to the semimajor axis velocity is f/ω. However, in a multidirectional wave field, differing propagation directions and phasing will rotate and change the ellipticity.

A unidirectional internal tide composed of several waves with different horizontal wavelengths will also have a transverse flux. From the polarization equations, we can calculate both the parallel ($\langle u'p' \rangle_{M_2}$) and transverse ($\langle v'p' \rangle_{M_2}$) flux averaged over a semidiurnal wave period. Both fluxes can be written in terms of a ratio between the two incident wavenumbers,

$$\frac{k_2}{k_1} = R_k. \tag{B4}$$

When $R_k = 1$, the two superposed waves are propagating in the same direction and have the same horizontal wavelength. When $R_k > 1$, both waves are propagating in the same direction, but the wavenumber k_2 is larger than k_1. Additionally, we shall make the magnitude of the two waves equal by setting $u_1 = u_2$ (if $u_1 \neq u_2$, one wave would dominate and the transverse flux is reduced; Martini et al. 2007). The parallel flux, oriented along the axis of propagation, becomes

$$\langle u'p' \rangle_{M_2} = u_1^2 \frac{\omega^2 - f^2}{2\omega k_1} \left(\frac{1 + R_k}{R_k} \right) \{1 + \cos[k_1(1 - R_k)x + (m_1 - m_2)z]\}, \tag{B5}$$

and the transverse flux, perpendicular to the axis of propagation, is

$$\langle v'p' \rangle_{M_2} = -u_1^2 \frac{f}{\omega} \frac{\omega^2 - f^2}{2\omega k_1} \left(\frac{1 - R_k}{R_k} \right) \sin[k_1(1 - R_k)x + (m_1 - m_2)z]. \tag{B6}$$

Both parallel and transverse fluxes have a periodic spatial structure with wavenumber $k_1(1 - R_k)$ (the difference between the horizontal wavenumbers) that are 90° out of phase, leading to spatial beating. Flux magnitude is also a function of the wavenumber ratio R_k. As k_2 increases and R_k goes to infinity, parallel flux magnitude decreases by half, and transverse flux magnitude is at a maximum. However, when the transverse flux is at a maximum, its magnitude is still a fraction of the parallel flux $[\langle v'p' \rangle_{M_2} / \langle u'p' \rangle_{M_2} = f(1 - R_k)/\omega(1 + R_k)]$. Although transverse fluxes occur when two waves of different wavelengths propagate in the same direction, it is always smaller by at least f/ω than the flux along the direction of propagation. Therefore, in a unidirectional wave field with waves of different wavelengths, the flux and semimajor current ellipse axis are still aligned along the direction of internal tide propagation.

Most internal wave fields are made up of many waves, each with different magnitude and direction. When multiple waves propagating in different directions are superposed, then flux will not necessarily be aligned along the semimajor axis. There are a limited number of cases where a multidirectional wave field can superpose to create what appears to be a unidirectional wave field. For example, two perpendicularly propagating internal tides of equal magnitude cause the flux and semimajor current ellipse axis to be aligned if phased correctly. Flux aligned along the semimajor axis of the current ellipse is not an absolute measure of unidirectionality but can still be used to determine the dominant direction of internal wave propagation, because often one wave is stronger than the others, causing observed fluxes and current ellipses to align along the propagation direction of the dominant wave.

REFERENCES

Alford, M. H., 2003: Redistribution of energy available for ocean mixing by long-range propagation of internal waves. *Nature,* **423,** 159–163, doi:10.1038/nature01628.

Althaus, A. M., E. Kunze, and T. B. Sanford, 2003: Internal tide radiation from Mendocino Escarpment. *J. Phys. Oceanogr.,* **33,** 1510–1527.

Bell, T. H., Jr., 1975: Topographically generated internal waves in the open ocean. *J. Geophys. Res.,* **80,** 320–327.

Cummins, P., J. Cherniawski, and M. Foreman, 2001: North Pacific internal tides from the Aleutian ridge: Altimeter observations and modeling. *J. Mar. Res.,* **59,** 167–191.

Desaubies, Y., and M. Gregg, 1981: Reversible and irreversible finestructure. *J. Phys. Oceanogr.,* **11,** 541–556.

Egbert, G. D., and S. Y. Erofeeva, 2002: Efficient inverse modeling of barotropic ocean tides. *J. Atmos. Oceanic Technol.,* **19,** 183–204.

——, and R. D. Ray, 2003: Semidiurnal and diurnal tidal dissipation from TOPEX/Poseidon altimetry. *Geophys. Res. Lett.,* **30,** 1907, doi:10.1029/2003GL017676.

Eriksen, C. C., 1982: Observations of internal wave reflection off sloping bottoms. *J. Geophys. Res.,* **87** (C1), 525–538.

——, 1985: Implications of ocean bottom reflection for internal wave spectra and mixing. *J. Phys. Oceanogr.,* **15,** 1145–1156.

——, 1998: Internal wave reflection and mixing at Fierberling Guyot. *J. Geophys. Res.,* **103** (C2), 2977–2994.

Fofonoff, N. P., 1969: Spectral characteristics of internal waves in the ocean. *Deep-Sea Res.,* **16,** 59–71.

Garrett, C., and E. Kunze, 2007: Internal tide generation in the deep ocean. *Annu. Rev. Fluid Mech.,* **39,** 57–87, doi:10.1146/annurev.fluid.39.050905.110227.

Gerkema, T., and H. van Haren, 2007: Internal tides and energy fluxes over Great Meteor Seamount. *Ocean Sci.,* **4,** 371–398.

Kelly, S. M., and J. D. Nash, 2010: Internal-tide generation and destruction by shoaling internal tides. *Geophys. Res. Lett.,* **37,** L23611, doi:10.1029/2010GL045598.

——, ——, and E. Kunze, 2010: Internal-tide energy over topography. *J. Geophys. Res.,* **115,** C06014, doi:10.1029/2009JC005618.

Kunze, E., 1985: Near-inertial wave propagation in geostrophic shear. *J. Phys. Oceanogr.,* **15,** 544–565.

——, L. Rosenfield, G. Carter, and M. C. Gregg, 2002: Internal waves in Monterey Submarine Canyon. *J. Phys. Oceanogr.,* **32,** 1890–1913.

——, E. Firing, J. M. Hummon, T. Chereskin, and A. Thurnherr, 2006: Global abyssal mixing inferred from lowered ADCP shear and CTD strain profiles. *J. Phys. Oceanogr.,* **36,** 1553–1576.

Leaman, K. D., and T. B. Sanford, 1976: Observations on the vertical polarization and energy flux of near-inertial waves. *J. Phys. Oceanogr.,* **6,** 894–908.

Ledwell, J. R., E. T. Montgomery, K. L. Polzin, L. C. St. Laurent, R. W. Schmitt, and J. M. Toole, 2000: Evidence for enhanced mixing over rough topography in the abyssal ocean. *Nature,* **403,** 179–182.

Legg, S., 2004: Internal tides generated on a corrugated continental slope. Part II: Along-slope barotropic forcing. *J. Phys. Oceanogr.,* **34,** 1824–1838.

MacKinnon, J. A., and K. B. Winters, 2005: Subtropical catastrophe: Significant loss of low-mode tidal energy at 28.9°. *Geophys. Res. Lett.,* **32,** LI5605, doi:10.1029/2005GL023376.

Marshall, J., A. Adcroft, C. Hill, L. Perelman, and C. Heisey, 1997: A finite-volume, incompressible Navier Stokes model for studies of the ocean on parallel computers. *J. Geophys. Res.,* **102** (C3), 5753–5766.

Martini, K. I., M. H. Alford, J. D. Nash, E. Kunze, and M. A. Merrifield, 2007: Diagnosing a partly standing wave in Mamala Bay, Oahu. *Geophys. Res. Lett.,* **34,** L17604, doi:10.1029/2007GL029749.

Merrifield, M. A., P. E. Holloway, and T. M. S. Johnston, 2001: The generation of internal tides at the Hawaiian Ridge. *Geophys. Res. Lett.,* **28,** 559–562.

Moum, J., D. Caldwell, J. Nash, and G. Gunderson, 2002: Observations of boundary mixing over the continental slope. *J. Phys. Oceanogr.,* **32,** 2113–2130.

Nash, J. D., E. Kunze, J. M. Toole, and R. W. Schmitt, 2004: Internal tide reflection and turbulent mixing on the continental slope. *J. Phys. Oceanogr.,* **34,** 1117–1134.

——, M. H. Alford, and E. Kunze, 2005: Estimating internal wave energy fluxes in the ocean. *J. Atmos. Oceanic Technol.,* **22,** 1551–1570.

——, E. Kunze, C. M. Lee, and T. B. Sanford, 2006: Structure of the baroclinic tide generated at Kaena Ridge, Hawaii. *J. Phys. Oceanogr.,* **36,** 1123–1135.

——, M. H. Alford, E. Kunze, K. Martini, and S. Kelly, 2007: Hotspots of deep ocean mixing on the Oregon continental slope. *Geophys. Res. Lett.,* **34,** L01605, doi:10.1029/2006GL028170.

Rainville, L., and R. Pinkel, 2006a: Baroclinic energy flux at the Hawaiian Ridge: Observations from the R/P *Flip*. *J. Phys. Oceanogr.,* **36,** 1104–1122.

——, and ——, 2006b: Propagation of low-mode internal waves through the ocean. *J. Phys. Oceanogr.,* **36,** 1220–1236.

Ray, R. D., and G. T. Mitchum, 1997: Surface manifestations of internal tides in the deep ocean: Observations from altimetry and island gauges. *Prog. Oceanogr.,* **40** (1–4), 135–162, doi:10.1016/S0079-6611(97)00025-6.

——, and D. E. Cartwright, 2001: Estimates of internal tide energy fluxes from TOPEX/Poseidon altimetry: Central North Pacific. *Geophys. Res. Lett.,* **28,** 1259–1262.

Rudnick, D. L., and Coauthors, 2003: From tides to mixing along the Hawaiian Ridge. *Science,* **301,** 355–357, doi:10.1126/science.1085837.

Simmons, H. L., R. W. Hallberg, and B. K. Arbic, 2004: Internal wave generation in a global baroclinic tide model. *Deep-Sea Res. II,* **51** (25–26), 3043–3068, doi:10.1016/j.dsr2.2004.09.015.

St. Laurent, L., and C. Garrett, 2002: The role of internal tides in mixing the deep ocean. *J. Phys. Oceanogr.,* **32,** 2882–2899.

——, S. Stringer, C. Garrett, and D. Perrault-Joncas, 2003: The generation of internal tides at abrupt topography. *Deep-Sea Res. I,* **50,** 987–1003, doi:10.1016/S0967-0637(03)00096-7.

Thurnherr, A. M., L. C. St. Laurent, K. G. Speer, J. M. Toole, and J. R. Ledwell, 2005: Mixing associated with sills in a canyon on the midocean ridge flank. *J. Phys. Oceanogr.,* **35,** 1370–1381.

Wunsch, C., 1968: On the propagation of internal waves up a slope. *Deep-Sea Res.,* **15,** 251–258, doi:10.1016/0011-7471(68)90002-8.

——, 1969: Progressive internal waves on slopes. *J. Fluid Mech.,* **35,** 131–144, doi:10.1017/S0022112069001005.

Zhao, Z., and M. H. Alford, 2009: New altimetric estimates of mode-1 M2 internal tides in the central North Pacific Ocean. *J. Phys. Oceanogr.,* **39,** 1669–1684.